

Self-regulated non-reciprocal motions in single-material microstructures

<https://doi.org/10.1038/s41586-022-04561-z>

Received: 22 October 2020

Accepted: 17 February 2022

Published online: 4 May 2022

 Check for updates

Shucong Li^{1,5}, Michael M. Lerch^{2,3,5}, James T. Waters⁴, Bolei Deng², Reese S. Martens², Yuxing Yao¹, Do Yoon Kim², Katia Bertoldi², Alison Grinthal², Anna C. Balazs⁴ & Joanna Aizenberg^{1,2}✉

Living cilia stir, sweep and steer via swirling strokes of complex bending and twisting, paired with distinct reverse arcs^{1,2}. Efforts to mimic such dynamics synthetically rely on multimaterial designs but face limits to programming arbitrary motions or diverse behaviours in one structure^{3–8}. Here we show how diverse, complex, non-reciprocal, stroke-like trajectories emerge in a single-material system through self-regulation. When a micropost composed of photoresponsive liquid crystal elastomer with mesogens aligned oblique to the structure axis is exposed to a static light source, dynamic dances evolve as light initiates a travelling order-to-disorder transition front, transiently turning the structure into a complex evolving bimorph that twists and bends via multilevel opto-chemo-mechanical feedback. As captured by our theoretical model, the travelling front continuously reorients the molecular, geometric and illumination axes relative to each other, yielding pathways composed from series of twisting, bending, photophobic and phototropic motions. Guided by the model, here we choreograph a wide range of trajectories by tailoring parameters, including illumination angle, light intensity, molecular anisotropy, microstructure geometry, temperature and irradiation intervals and duration. We further show how this opto-chemo-mechanical self-regulation serves as a foundation for creating self-organizing deformation patterns in closely spaced microstructure arrays via light-mediated interpost communication, as well as complex motions of jointed microstructures, with broad implications for autonomous multimodal actuators in areas such as soft robotics^{7,9,10}, biomedical devices^{11,12} and energy transduction materials¹³, and for fundamental understanding of self-regulated systems^{14,15}.

Self-regulation is fundamental to complex motion in living systems, but how to design for and harness such emergent behaviour in microscale synthetic materials is not yet well understood. In biology, self-regulated responses emerge from multiple levels of integrated feedback, both within the system and in turn within the stimulus field, intricately orchestrating dynamic movement trajectories with spatial and temporal complexity that are rarely seen in synthetic actuators. For most complex microscale motions demonstrated so far, each position along a trajectory must be either explicitly programmed into the material through fabrication^{4,7,16–19} or directly manipulated in real time by sequential change of external stimuli^{3,5,17,20,21}. Feedback incorporated into materials, for example by multilayer, hierarchical or multi-stimuli-responsive compositions^{22–24}, or embedded chemical reactions and patterning^{25,26}, has led to unique actuation modes or temporal dynamics, but the achieved motions are still largely defined by the underlying architecture or oscillatory dynamics^{27–29}, resulting in a limited set of highly specific, generally two-state movements, with little dynamic pathway control. Harnessing feedback with a stimulus, such

as light or a magnetic field, enables dynamic amplification of phototropic^{25–30} or other behaviours, but without internal feedback it remains difficult to programme complex or diverse motion trajectories into microscale artificial systems. To take self-regulated motion to the next level, both internal and external feedback from a full three-dimensional (3D) space must be integrated, but current trends in addressing this challenge by engineering ever more complexity into hierarchical multimaterial constructs may—in addition to being technically complicated—inadvertently narrow opportunities for the spontaneous, bottom-up self-integration seen in living systems.

Here we introduce an orthogonal approach to this trend and design simple, compositionally uniform microstructures capable of a vast set of self-regulated motions. We focus on molecularly anisotropic materials that: (1) are aligned non-collinearly to the principal axis of the microstructure; and (2) undergo a stimulus-induced order-to-disorder transition. We hypothesized that these two basic design requirements must be met to invoke and interweave multiple levels of feedback. For example, consider a photosensitive micropost illuminated by a

¹Department of Chemistry and Chemical Biology, Harvard University, Cambridge, MA, USA. ²John A. Paulson School of Engineering and Applied Sciences, Harvard University, Cambridge, MA, USA. ³Stratingh Institute for Chemistry, University of Groningen, Groningen, the Netherlands. ⁴Chemical Engineering Department, University of Pittsburgh, Pittsburgh, PA, USA. ⁵These authors contributed equally: Shucong Li, Michael M. Lerch. ✉e-mail: jaiz@seas.harvard.edu

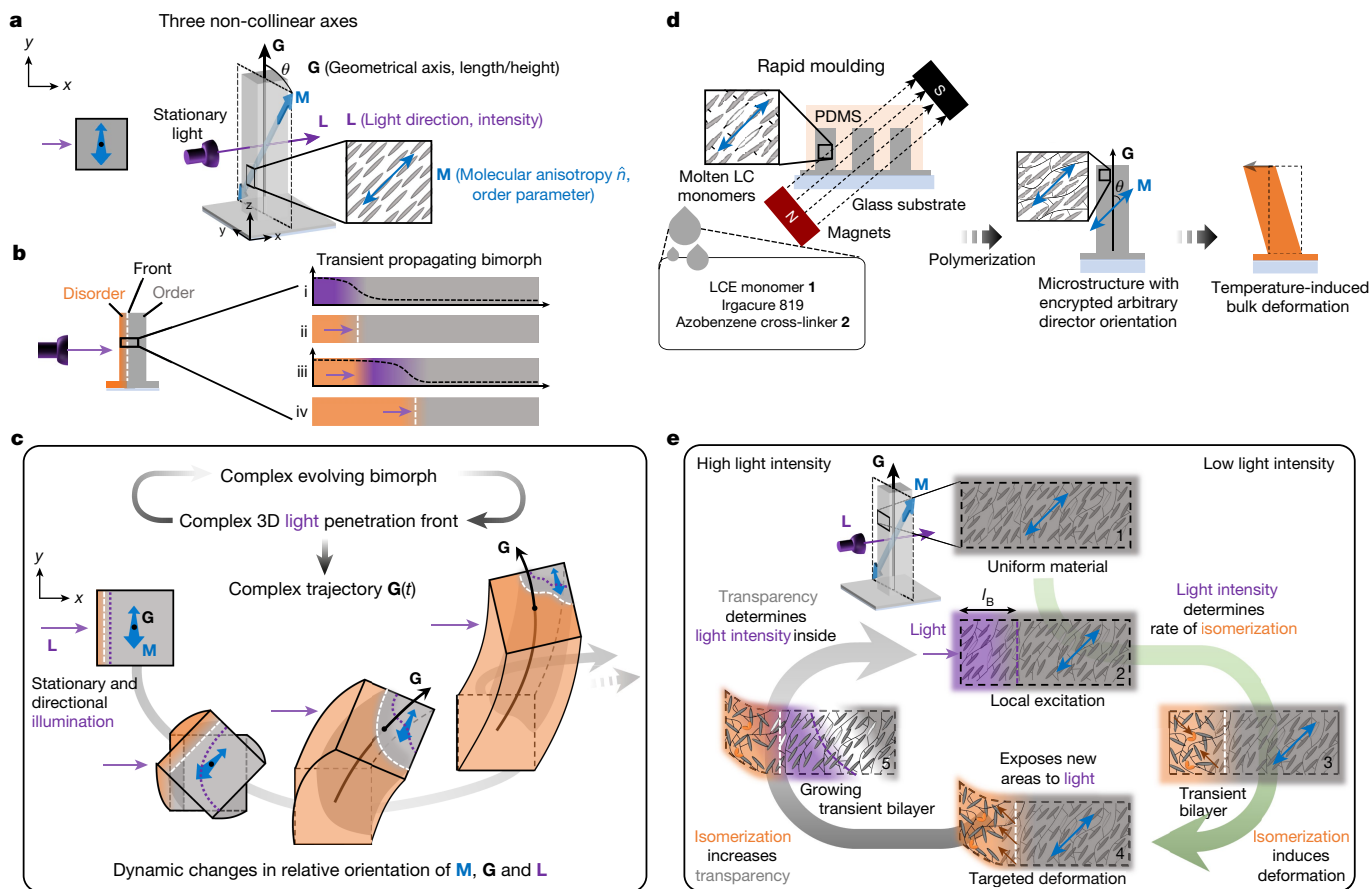


Fig. 1 | Three non-collinear symmetry axes and their dynamic opto-chemo-mechanical feedback enable an infinite set of self-regulated motions in a compositionally uniform microstructure. **a**, Misalignment of molecular anisotropy (**M**), microstructure geometry (**G**) and light (**L**)—each with programmable directionality and magnitude—lays the basis for spatiotemporally diverse microstructure deformation trajectories. **b**, A transient bimorph is formed in a single material by directional light activation (orange represents ‘activated’ and disordered; grey, ‘non-activated’ and ordered) with a stationary light source. The order-to-disorder front (indicated by a white dashed line) self-propagates via induced transparency and leads to a dynamically evolving bimorph: directional illumination (i) locally triggers order-to-disorder transition (ii), which increases the material’s transparency and enables light to penetrate deeper into the structure (iii), resulting in a travelling disorder-to-order front (iv). **c**, Complex deformation trajectory, represented by the changing orientation of $\mathbf{G}(t)$, is produced by feedback between bimorph evolution, complex 3D light penetration profile and the corresponding dynamic

stationary light source, such that the system’s three primary symmetry elements (molecular anisotropy, **M**, geometrical axis, **G**, and illumination direction, **L**) are all linearly independent in 3D (Fig. 1a). As light enters and triggers a chemically driven order-to-disorder transition in a thin layer of the material, the structure will transiently become a bimorph, in which an initially thin ‘activated’ disordered region (shown in orange) is assumed to self-propagate by induced transparency^{30,31} (Fig. 1b). At the molecular scale, the order-to-disorder transition will generate a directional force normal to—and determined solely by—the initial molecular alignment direction. The subsequent structural deformation will be determined by a combination of this directional force and the orientation of the bimorph interface relative to the principal structure axis (Fig. 1c, left). These combined forces drive the post to bend and twist, and thereby expose different faces to the light. Due to this mechanical motion, the direction of molecular alignment will reorient relative to the illumination direction, creating an increasingly

reorientations among the **MGL** axes. **d**, High-aspect ratio microposts are moulded from a photoresponsive liquid crystalline elastomer (LCE; LCE monomer **1**: 4′-acryloyloxybutyl) 2,5-di(4′-butyloxybenzoyloxy)benzoate; cross-linker **2**: 4,4′-bis(9-acryloyloxynonyloxy) azobenzene; photoinitiator Irgacure 819; bis(2,4,6-trimethylbenzoyl)-phenylphosphine oxide), and molecular anisotropy is pre-oriented along an arbitrary direction by a magnetic field before polymerization. A photoswitchable azobenzene cross-linker confers light-sensitive disruption of molecular order. Curing of the elastomer locks in the magnetically programmed molecular anisotropy within the microstructure. The liquid crystal (LC) director orientation (denoted by the blue double arrow) determines the bulk deformation. **e**, An opto-chemo-mechanical feedback loop modulates the transiently activated region and is key to complex micropost motion. Both the change in transparency and the material deformations change the light intensity inside the material over time, which then induces further isomerization and deformation.

complex travelling front (shown by the dotted purple line in Fig. 1c), which will continuously reorient the principal geometric axis $\mathbf{G}(t)$, enabling the microstructure to flow seamlessly among various deformation modes. Although the overall photoinduced transition is fully reversible, the specific iterative pathway of bimorph evolution is not, enabling inherently non-reciprocal stroke-like motions.

To test the hypothesis and design a representative system, we start with the simple geometry of a high-aspect-ratio square micropost (height = 150 μm ; side lengths = 30 μm) (Supplementary Fig. 1). Molecular anisotropy within the micropost was achieved by using liquid crystalline elastomers (LCEs)^{32,33} with the director pre-aligned in an arbitrary orientation using a magnetic field^{34,35} (Fig. 1d, Supplementary Figs. 2–4, Supplementary Methods). Such molecular programmability is distinct from the majority of fabrication methods, which involve either mechanical processing (such as shearing, stretching and 3D printing) in which the LCE director is always parallel to the principal

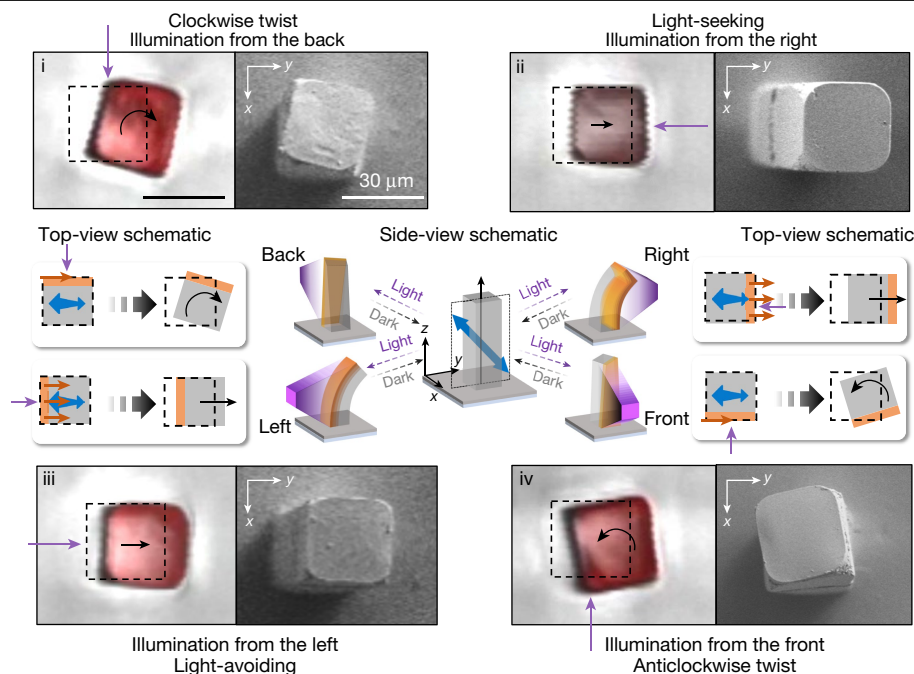


Fig. 2 | In a micropost with oblique director alignment, distinct elementary deformation modes are evoked by irradiation from different directions.

Confocal laser scanning and scanning electron microscopy images of actuated photoresponsive LCE microposts with oblique director alignment of $\theta \approx 55^\circ$ (tilted with respect to the principal axis into the yz plane) upon UV irradiation (15 mW cm^{-2}) of four facets (i, 'back'; ii, 'right'; iii, 'left'; and iv, 'front'). The top-view schematics explain the observed deformation behaviour resulting

from the molecular orientation-induced shearing of the active (orange) layer, which exerts clockwise torque, pull and push, and anticlockwise torque, on the inactive layer, leading to clockwise twisting, bending towards light, bending away from light and anticlockwise twisting of the same microstructure for i–iv, respectively. Director orientation is depicted as a blue double arrow; shear forces are depicted as orange arrows and the resulting movements as black arrows, respectively. Purple arrows indicate illumination direction.

symmetry axis of the microstructure^{19,36–38}, or surface alignment with complex director orientations, but which are only applicable to thin films^{28,29,39}. (Note that magnetic field is only used during the fabrication and not in the subsequent actuation process.) An azobenzene cross-linker was chosen to elicit photomechanical actuation (Fig. 1d, Supplementary Fig. 5), which provides high spatial resolution at the microscale as opposed to the more commonly employed photothermal mechanism (Supplementary Figs. 6, 7)^{40,41}. On exposure to ultraviolet (UV) radiation, azobenzene cross-linkers undergo reversible *trans*-to-*cis* photoisomerization, which mechanically disrupts the local molecular order^{4,41} to create a temporary bimorph inside the post, consisting of an 'activated' disordered layer and a 'non-activated' nematic phase, as discussed above. We chose a relatively high⁴⁰ concentration of azobenzene cross-linker (7.5 wt%), which restricts light penetration ($\lambda_{\text{max}} = 365 \text{ nm}$) initially to a depth l_B of a few micrometres at mild UV intensity (approximately 15 mW cm^{-2}) according to the Beer–Lambert law $I/I_0 \propto e^{-\varepsilon cl}$ (l_B defined as l at $1/e$ of I_0 with incident light intensity I_0 , molar attenuation coefficient ε and concentration c of the light-absorbant species). Changing the light intensity influences the penetration depth l_B within the post, and the rate with which a photostationary state between the *trans*- and *cis*-isomer is established. Notably, when the light intensity is sufficiently large, a high photostationary state rapidly forms within the first few micrometres, increasing the UV transparency and deepening UV penetration to enable further order-to-disorder conversion of deeper layers, thus creating a travelling isomerization wave^{30,31}. In thin films, such a propagating isomerization front is well known to result in one deformation type—bending towards the light followed by a reversal of direction to an equilibrium position^{30,31} (Supplementary Fig. 8, Supplementary Video 1)—whereas, as we will show below, diverse deformations with non-reciprocal trajectories appear in the system with programmed non-collinear principal axes.

To quantitatively predict the complex opto-chemo-mechanical dynamics and corresponding deformation trajectories of microstructures as a function of the molecular orientation in the constituent LCE material (**M**), the microstructure geometry (**G**) and the direction of illumination (**L**), as well as the light intensity (Fig. 1a), we developed a computational model based on a finite element approach (Supplementary Model 1). The model integrates all the dynamic processes regulating the system (Fig. 1e): the light penetrating into the material, the resultant intensity-dependent photoisomerization and the consequent localized change in the nematic order parameter. The model further couples the order parameter to the strain of the material and reveals the time-dependent evolution of the light-generated bimorph. In this way, it allows us to study and predict in detail how these dynamic processes interact to create the compounding complexity of the deformation pathways. Informed by our finite element model, we demonstrate how these feedback mechanisms make the system amenable to high-resolution programming of diverse motion trajectories, by varying initial conditions, including illumination direction, director orientation, light intensity, microstructure geometry and temperature, and/or by modulation of illumination intervals and duration, as well as extending it to cooperative movements in microstructure arrays and more complex microstructure geometries.

Illumination direction

The unique combination of three non-collinear directional elements (**MGL**) present in our system breaks symmetry differently for each angle of illumination and evokes distinct elementary deformation modes. We experimentally demonstrate four such modes for a chemically uniform microstructure with oblique director illuminated from four sides⁴². As defined by the director, the illuminated 'activated' (orange) slab always undergoes a shear, which, depending on the facet of the micropost being illuminated, exerts push/pull forces or clockwise/anticlockwise

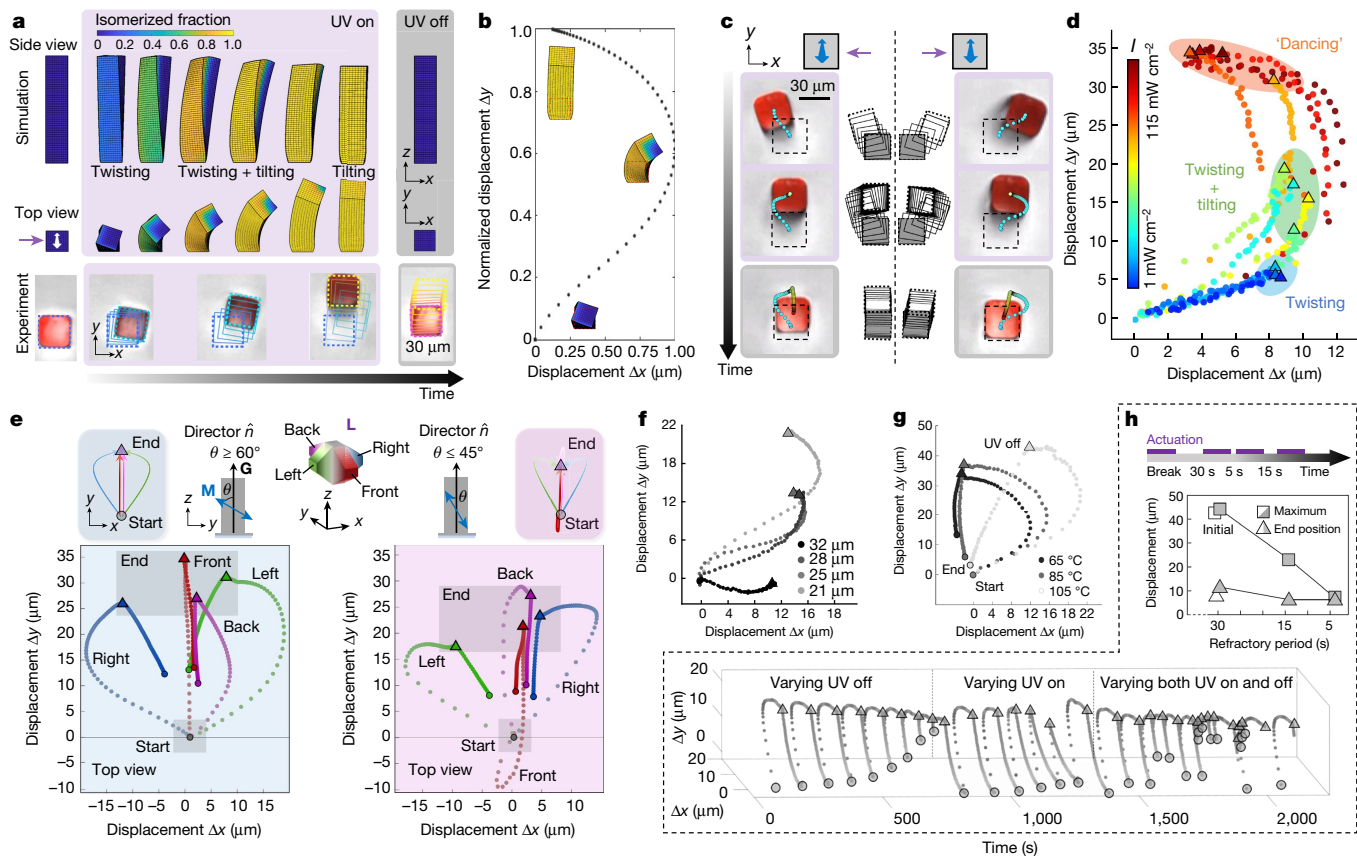


Fig. 3 | High-resolution programming of diverse stroke-like motions. **a**, Juxtaposed computationally simulated (top two rows) and experimental (bottom) data capturing the travelling isomerization wave^{30,31} and complex evolving bimorph resulting from the *trans*- (blue) to *cis*- (yellow) photoisomerization of the azobenzene cross-linker, leading to a stroke-like deformation of the microstructure with oblique director alignment ($\theta = 52^\circ$) at high-intensity illumination (115 mW cm^{-2}). Simulation results were rescaled in time for the experiment. Image tracking overlaid on experimental data (confocal laser scanning microscopy still images, Supplementary Fig. 12) illustrates the deformation trajectory. In image tracking, photoactuation is depicted by the blue-to-yellow transition and thermal relaxation by the yellow-to-red transition. **b**, Predicted normalized deformation trajectory for case in **a** accompanied by top-view rendered simulation still images. **c**, For out-of-plane irradiation (115 mW cm^{-2}) from opposite sides, the same microstructure displays mirrored right- and left-handed curved stroke-like trajectories. **d**, Experimental quantification of different deformation trajectories for 12 light intensities in the range $1\text{--}115 \text{ mW cm}^{-2}$. Circles correspond to the trajectories of the micropost's centre of the top surface during deformation; triangles denote a stable deformed position reached at

the photostationary state. **e**, The director tilt (θ) modulates the relative contribution of the shearing component (along the y axis) and contraction/expansion (along the z axis). Experimental deformation trajectories and their schematic representation for two cases ($\theta = 60^\circ$ and $\theta = 45^\circ$) for UV irradiations from the front (red), left (green), back (magenta) and right (blue) are shown. Note 'dancing' towards or away from the light source, respectively, as is observed by the switch between the green and blue trajectories for the two cases. **f, g**, Effect of microstructure thickness (**f**) and temperature (**g**) on deformation trajectories. **h**, The non-instantaneous *cis*-to-*trans* thermal relaxation of the azobenzene cross-linker causes a refractory period between two illumination periods. Top panel illustrates the reduced deformation amplitude with decreasing length of time breaks. Squares correspond to maximum displacement; triangles denote displacement before switching UV off. Bottom panel shows 3D traces of deformation paths along both x and y directions as a function of time under varied illumination duration and intervals, demonstrating deliberately tailored beginning and end points of each actuation path. Circles correspond to starting point of each illumination; triangles denote displacement before switching the UV irradiation off.

torques on the 'non-activated' (grey) layer, giving rise to light-seeking, light-avoiding and clockwise or anticlockwise twisting, respectively (Fig. 2, Supplementary Figs. 9–11, Supplementary Video 1). By contrast, heating the structure shows only direct tilting (Supplementary Fig. 10b), as expected for a micropost with an oblique director undergoing a bulk nematic-to-isotropic phase transition. Once the light is switched off, the post directly returns to its original state, because the *cis*-isomer⁴³ is thermally unstable (thermal half-life was determined to be $t_{1/2} = 40 \text{ s}$ in the LCE film at 60°C) (Supplementary Fig. 5).

Illumination intensity

Our finite element model (Supplementary Model 1) shows how, at higher light intensity, multiple types of such motional elements transition seamlessly from one to another through opto-chemo-mechanical

feedback, with complex evolution of the bimorph influencing each subsequent step, as exemplified here in a predicted stroke-like trajectory of a single micropost (Fig. 3a, b): (i) the structure initially twists as a thin illumination layer emerges, which immediately exposes the adjacent new facet to the light; (ii) as the light penetrates further from both facets into the structure, the 'push' force and clockwise twist synergistically move the micropost diagonally away from its initial structural axis; and (iii) as the illuminated region grows and starts to take up a majority of the bimorph, backwards bending begins towards a simply tilted micropost, as defined by its nematic director; (iv) when the light is switched off, the structure undergoes a uniform disorder-to-order transition, tilting directly back upright to its initial position, completing a non-reciprocal deformation pathway. We experimentally achieved such self-regulated highly non-linear 'dancing' actuation under high

irradiation intensity of 115 mW cm^{-2} (Fig. 3a, bottom, Supplementary Figs. 12, 13, Supplementary Video 2).

When the square micropost is illuminated under high intensity (115 mW cm^{-2}) from either one or the other direction along, for example, the x axis, an identical end position (tilting) governed by the oblique director is achieved when light penetrates through the entire structure (reminiscent of the bulk thermal nematic-to-isotropic phase transition), but mirrored, right- and left-handed, stroke-like actuation paths towards this final state are observed (Fig. 3c, Supplementary Video 3). Movement of the pillar along these trajectories can be further controlled by changing light intensity, which determines where the evolving order–disorder bimorph stabilizes, and, hence, the net force exerted on the post. Figure 3d quantifies these effects at 12 light intensities ($1\text{--}115 \text{ mW cm}^{-2}$) (Supplementary Figs. 13, 14), showing that the same micropost can undergo the twisting motion at lower intensities (as in Fig. 2), but smoothly transitions from twisting to tilting at medium light intensity, and then evolves into an asymmetric, stroke-like movement (‘dancing’) involving both twisting and tilting outward and inward at maximum light intensity, a behaviour accurately predicted and captured by our simulations (Supplementary Video 2).

Director tilt

We have developed a model that describes how the angle of molecular alignment with respect to the post’s geometrical axis (θ) affects the microstructure deformation along the vertical and horizontal directions (Supplementary Model 2, Supplementary Figs. 15, 16). Although the horizontal component is important for shearing within the bimorph, exerting torques and causing twisting motions, the vertical component independently contributes to out-of-plane bending within the trajectory and can be chosen to be either toward ($\theta \geq 60^\circ$) or away from the light ($\theta \leq 45^\circ$) (Fig. 3e). This will lead to ‘dancing’ toward or away from the light source, respectively. Furthermore, for steep director alignments ($\theta \leq 45^\circ$), a characteristic reversal of motion along the yz plane is observed (Supplementary Figs. 17–19).

Microstructure size

The thickness of the micropost influences not only its effective mechanical stiffness and thus the deformation amplitude, but also the relative size of the ‘activated’ layer in the evolving bimorph and thus the deformation trajectory (Fig. 3f, Supplementary Fig. 20, Supplementary Video 4). For thicker posts, the out-of-plane movement dominates over the shearing movement and the propagating order-to-disorder transition fades out quickly, leading to a distinctly different deformation trajectory and end point.

Temperature

Simply changing the temperature at which the structure is illuminated provides further methods for high-resolution programming of the motion trajectory. An increase in temperature reduces the material stiffness, which usually enhances deformation amplitude. At the same time, a higher temperature also speeds up the azobenzene *cis*-to-*trans* thermal relaxation, lowering the photostationary state reached and increasing the fraction of the *trans*-azobenzene corresponding to reduced UV transparency. Hence, the progression of the travelling isomerization front stops earlier. These two effects work synergistically to influence the actuation trajectory (Fig. 3g, Supplementary Fig. 21, Supplementary Video 4) to a larger out-of-plane motion. Note that ample means are available for speeding up the deformation by decreasing the thickness of the micropost, lowering the concentration of the azobenzene cross-linkers or extending to other photochemistries³³.

Irradiation duration and intervals

As discussed, the activated photoswitchable cross-linker thermally returns to its *trans*-isomer within the LCE, and the microstructure relaxes to its original upright state within seconds to minutes after

the light is switched off. If irradiation is renewed during this ‘refractory period’ when a majority of azobenzene cross-linkers is still in the *cis*-form, only marginal deformation occurs. Leveraging this effect, the starting and end position, as well as the amplitude of the arc and path of relaxation of the deforming pillar, can be precisely chosen by controlling the illumination duration and intervals, producing a rich ‘dancing’ behaviour with no noticeable fatigue for over 100 cycles (Fig. 3h, Supplementary Figs. 22–24, Supplementary Video 5).

Cooperative movements in arrays of microstructures

As one expands the system from a single micropost to strings of microstructures or two-dimensional (2D) arrays (produced by a simple moulding procedure), additional symmetry axes (degrees of freedom) are added to the system, which in the simplest case of a one-dimensional (1D) array can be captured by the array axis \mathbf{G}_a defined in terms of a string direction and interpillar distance, w . We explored the potential for dynamic pattern evolution and emergent communication between the microstructures in such a system using a string of circular microposts with z -aligned mesogens (\mathbf{G} and \mathbf{M} collinear) (Fig. 4a–d). If \mathbf{G}_a and \mathbf{L} are perfectly aligned, one would expect only bending towards the light (along the string axis) with rapidly decreasing amplitude. However, as schematically presented in Supplementary Fig. 25, with even a small misalignment between \mathbf{G}_a and \mathbf{L} (shown as angle δ), the first pillar would bend slightly out of line, leading to asymmetric exposure of the next pillar and creating a bimorph that bends out of the string axis in an opposite direction, with bending amplitude and symmetry breaking amplified along the string in a distance- and location-dependent manner. To capture such a unique collective response in pillar arrays, we developed a simplified discrete model that considers how the interpillar communication changes what parts of neighbouring microstructures become illuminated on directional light exposure (Supplementary Model 3, Supplementary Fig. 26). Our simulations, confirmed by the follow-up experiments, show that in pairs of z -aligned microposts of different interpost spacing w ($w = 45, 65$ or $130 \mu\text{m}$), for a small δ , symmetry breaking arises at $w = 65 \mu\text{m}$, whereas at short distances no actuation of the mostly shadowed second post occurs and at long distances ‘decoupled’, identical bending towards the light of both posts is observed (Fig. 4a). In longer strings, such distance-dependent symmetry breaking leads to a stable and repeatedly reproducible wave-like pattern (Fig. 4b), a behaviour accurately captured by both our finite element simulations (Supplementary Fig. 27) and a simplified mathematical model (Fig. 4b, right). The spontaneous asymmetry amplification endows the system with a high sensitivity to any $\mathbf{G}_a\mathbf{LM}$ non-collinearity and access to drastically different self-sorted patterns (Supplementary Figs. 28, 29, Supplementary Video 6). The degree of interpillar coupling and thus self-organization depends strongly on the magnitude of misalignment, δ , most effectively demonstrated in a 2D square array of microposts containing \mathbf{G}_a (axis along the nearest neighbour) and $\mathbf{G}_{a,d}$ (direction along the diagonal) axes. As the array is illuminated along the \mathbf{G}_a or $\mathbf{G}_{a,d}$ direction, the effective interpost spacing changes, thus enhancing or suppressing the interpost communication (Fig. 4c, Supplementary Video 7).

We further note that under conditions that allow for dynamic bimorph propagation locally within each single pillar (as described in Fig. 3), a unique, ‘global’ deformation front is expected to travel concurrently at the ensemble level (with a different propagation velocity) dependent on the effective pillar density along the light path. Indeed, we showcase in a radially arranged microarray with z -aligned mesogens (Fig. 4d) that when the array is illuminated, these interacting propagation fronts lead to a complex evolution of the travelling wave of the communicating posts at the ensemble level. In this radial arrangement, the multiple \mathbf{G}_a axes have different relative orientations to \mathbf{L} , resulting in various local hierarchical spacings along the light path and causing the complexity of the collective travelling front (Supplementary Video 7). Moreover, if \mathbf{G} and \mathbf{M} are non-collinear within each micropost, one would expect that in a 2D array, the previously described

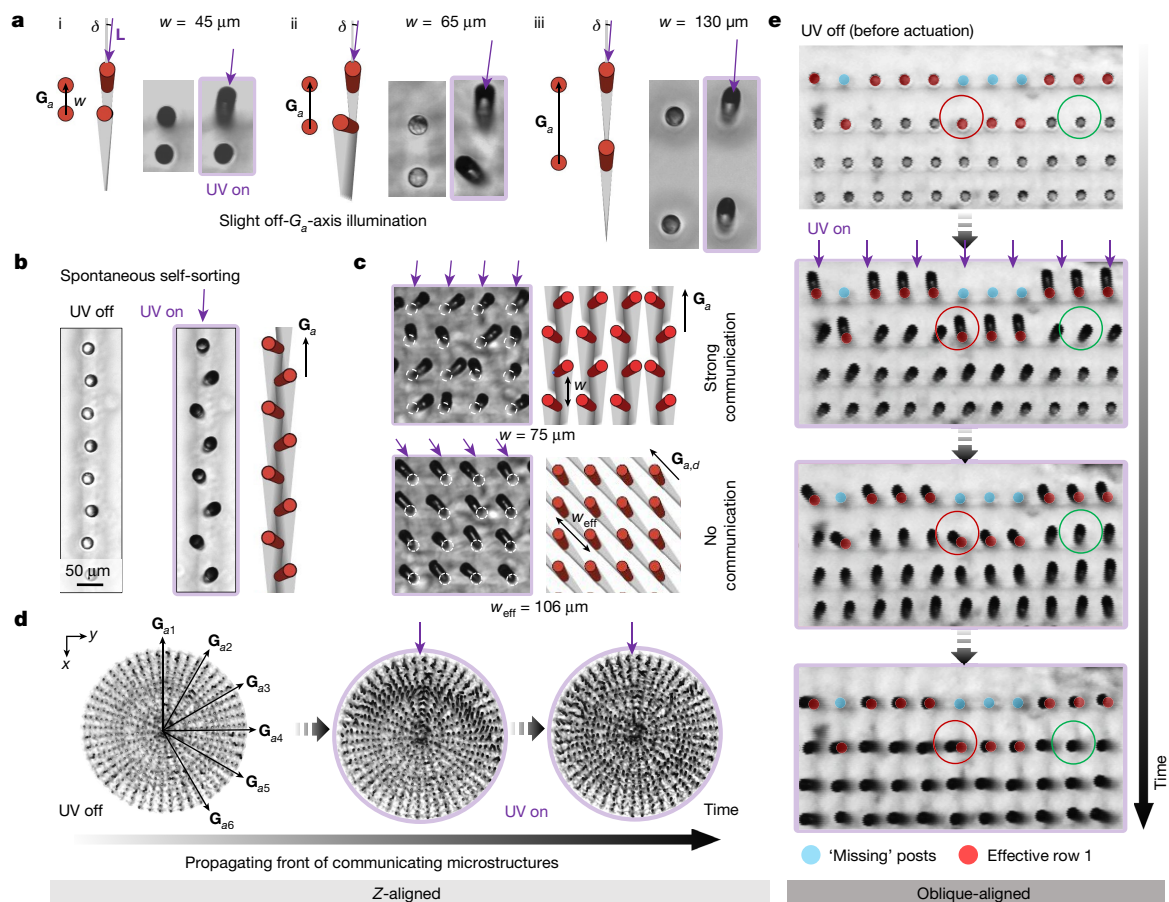


Fig. 4 | Collective self-regulated deformation dynamics in arrays of microposts. **a**, Simulation (left) and experimental (right) results of the light response of pairs of microposts, when the illumination direction, L , forms a small angle, δ , with the pair axis, G_a , illustrating how different interpost spacings, w , influence the deformation trajectory of subsequent posts. **b**, Spontaneous self-organization of appropriately spaced strings of microposts into an undulating line. Modelling results are shown on the right. **c**, For a square 2D microarray, strong interpost communication and coupled undulating deformations occur when light comes along the nearest neighbour

direction (G_a , $w = 75 \mu\text{m}$), and decoupled uniform light-seeking motions when illuminated along the diagonal ($G_{a,d}$, $w = 106 \mu\text{m}$). Left: experiment; right: simulation. **d**, Formation of a complex travelling wave of locally interacting posts in a radially arranged microarray, demonstrating a rich ensemble dynamics. **e**, Amplification of engineered 'defects' in arrays of oblique-aligned microposts: missing microstructures alter the local illumination conditions and interpillar spacing and change the deformation trajectories of the posts around them, and thus the overall ensemble dynamics. Optical microscopic images of the illuminated posts in **a–e** are outlined in purple.

'dancing' motions of each post would adapt to and self-organize with the motion of their neighbours, with each post undergoing a unique position-dependent trajectory (Supplementary Fig. 30). Together with programmed defects (for example, missing pillars), one can therefore construct micropost ensembles with highly controlled, emergent time- and location-dependent deformation trajectories (Fig. 4e). For example, two microposts (circled in red and green) from the same row in the array exhibit completely different deformation trajectories yet start and end at similar states (Fig. 4e, Supplementary Video 8).

More complex geometries

In free-standing, jointed, compositionally uniform microstructures, the presence of multiple geometrical axes (in this case G_{segment} , the principal symmetry axis of each constitutive part) provides additional opportunities for cooperative complex deformation patterns, such as stirring, bowing or bird-like motions, arising from distinct relative G_{segment} orientations and thus distinct local symmetry breakings and corresponding motions for each constitutive part. For example, an X-shaped actuator exhibits programmable deformations that include mutually opposite right- and left-handed twisting and bending of the G_{segment}^{13} and G_{segment}^{24} reminiscent of crawlers or the wing-warping/twisting necessary for bird flight (Fig. 5a, Supplementary Figs. 31–33, Supplementary Video 9). The helicity and extent of

twisting and closure/opening or out-of-plane movements of the arms can be judiciously chosen through variations of relative orientations of L , M and geometrical axes of each arm. By contrast, thermal heating of the X-shaped actuator shows only one deformation—a direct shrinkage along the molecular alignment to a 'slender' X without undergoing any twisting (Supplementary Fig. 34). Furthermore, if one end of the arm (G_{segment}^{13}) now serves as an anchoring point, a greatly amplified twist of G_{segment}^{24} fully coupled to the motion of G_{segment}^{13} is observed. This implies that such actuators can serve as micro-joints/hinges with the ability to control a variety of motion trajectories of macroscale pieces. Our computational method enables us to further explore a library of combinations of G_{segment} and show deformations, including 'stirring', and catching or releasing cargo (Supplementary Video 10). As an illustration, Fig. 5b models diverse motions of T-, L- and palm-tree-shaped compositionally uniform actuators undergoing multiple, evolving in time, deformations depending on the light direction. Non-symmetrical movements of different arms can be readily achieved by shifting the illumination direction away from the structure-symmetric axes or having off-axis director orientation (Supplementary Fig. 35). The ramifications for microscopic soft robots capable of a tremendous set of motions are immediate and numerous.

To conclude, we present a strategy for programming various self-regulated, stroke-like dancing trajectories in a single,

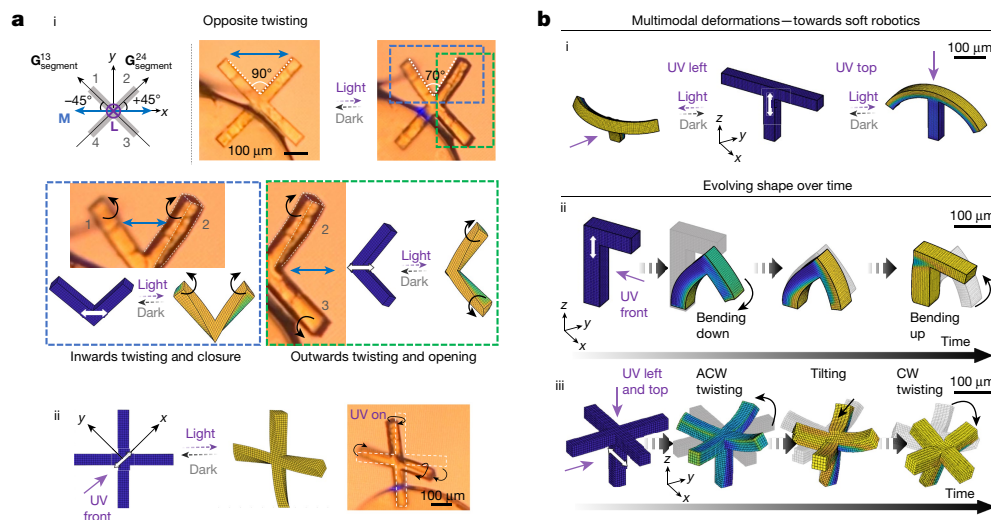


Fig. 5 | Higher order self-regulated dynamics in jointed compositionally uniform microactuators. **a**, i, In a free-standing X-shaped actuator containing two perpendicular structural axes $G_{segment}^{13}$ and $G_{segment}^{24}$, which form $+45^\circ$ and -45° with the uniform director orientation, M (shown as a blue double arrow), bending and twisting motions of opposite direction can be invoked for different arms within the same single-material, moulded microstructure. Magnified photographs and corresponding theoretical simulations depicting the motion of the top two and the right two segments of the structure are shown below in blue and green insets, respectively. ii, With one arm being the anchoring spot, the twisting of $G_{segment}^{24}$ couples to the twisting/rotation of the

$G_{segment}^{13}$ axis, demonstrating amplification of the sway motion through the arms in both simulations and experiments. **b**, Simulation results for diverse motions in: (i) T-shape with global vertical molecular alignment that undergoes distinct deformations for different light directions (i); L-shape actuator with global vertical molecular alignment, illustrating a programmable movement sequence of bending down and upwards in a single UV actuation period, as a travelling light front propagates through the structure (ii); palm-tree-shaped actuator with oblique molecular alignment, illustrating a progressive anticlockwise (ACW) and clockwise (CW) twisting accompanied by the closure and opening of the arms (iii).

compositionally uniform microstructure fabricated by a simple moulding procedure. The self-regulatory behaviour is fundamentally different from existing feedback systems: due to the imposed non-collinearity of **MLG** axes, light propagating through the material generates a transient, dynamically evolving bimorph with increasingly complex symmetry breaking along the front, specifying a diversity of motion pathways composed of different deformation types—composites of twisting, bending, light seeking and light avoiding. The resulting range of actuations cannot be achieved with existing approaches that involve complicated multimaterial architectures, 3D printing or direct manipulation, especially for 3D structures in the 10–100 μm size range. Our simulations quantitatively capture this multilevel opto-chemo-mechanical feedback dynamics, enabling us to theoretically predict and experimentally programme the spatiotemporal behaviour of nearly infinite actuation pathways. The core design principles presented here can be applied to other anisotropic materials, such as fibre-reinforced hydrogels^{44,45} or shape-shifting crystals⁴⁶, and extended to include different photochemistries³³, and polarized or dynamic light sources.

Furthermore, this self-regulated bimorph dynamics has marked implications for eliciting complex collective behaviours in microstructure arrays, in which **MLG** reorientations involving additional geometrical axes (G_{array}) lead to distinct position-dependent symmetry breaking and unique motion pathways for each micropost. The interpillar communication and multilevel propagation dynamics we demonstrate reveal the fundamental scalability and predictability of the designed feedback mechanism beyond a single microstructure, and provide the means to control the collective behaviour in microstructure ensembles. The observed emergent behaviours, such as bistability, stable wave-like patterns and sensitivity to small perturbations, are typically hallmarks of complexity⁴⁷ in multicomponent systems that rely on molecular-scale, diffusion or flow-limited processes, such as chemical reaction networks^{48–50} or even chemo-mechanical actuators^{27,28}, but here complexity emerges from the simplicity of the single-material photoresponsive system. The design concepts introduced herein also lead to bird-like

and other complex programmed motions in free-standing jointed single-material microstructures with multiple non-aligned $G_{segment}$ axes. This vast design space for individual and collective motions is potentially transformative for fields ranging from soft robotics, micro-walkers, sensors and cell culture scaffolds to robust information encryption systems in which information encoded in an array can be read out by an infinite number of different dynamic patterns evoked by different illumination directions, intensities, durations, intervals, as well as wavelengths and polarizations.

Online content

Any methods, additional references, Nature Research reporting summaries, source data, extended data, supplementary information, acknowledgements, peer review information; details of author contributions and competing interests; and statements of data and code availability are available at <https://doi.org/10.1038/s41586-022-04561-z>.

- Sleigh, M. A. *The Biology of Cilia and Flagella* (Pergamon Press, 1962).
- Gilpin, W., Bull, M. S. & Prakash, M. The multiscale physics of cilia and flagella. *Nat. Rev. Phys.* **2**, 74–88 (2020).
- Hu, W., Lum, G. Z., Mastrangeli, M. & Sitti, M. Small-scale soft-bodied robot with multimodal locomotion. *Nature* **554**, 81–85 (2018).
- Van Oosten, C. L., Bastiaansen, C. W. M. & Broer, D. J. Printed artificial cilia from liquid-crystal network actuators modularly driven by light. *Nat. Mater.* **8**, 677–682 (2009).
- Gu, H. et al. Magnetic cilia carpets with programmable metachronal waves. *Nat. Commun.* **11**, 2637 (2020).
- Rus, D. & Tolley, M. T. Design, fabrication and control of soft robots. *Nature* **521**, 467–475 (2015).
- Huang, H. W., Sakar, M. S., Petruska, A. J., Pané, S. & Nelson, B. J. Soft micromachines with programmable motility and morphology. *Nat. Commun.* **7**, 12263 (2016).
- Wu, Z. L. et al. Three-dimensional shape transformations of hydrogel sheets induced by small-scale modulation of internal stresses. *Nat. Commun.* **4**, 1586 (2013).
- Tottori, S. et al. Magnetic helical micromachines: fabrication, controlled swimming, and cargo transport. *Adv. Mater.* **24**, 811–816 (2012).
- Wehner, M. et al. An integrated design and fabrication strategy for entirely soft, autonomous robots. *Nature* **536**, 451–455 (2016).
- Yan, X. et al. Multifunctional biohybrid magnetite microrobots for imaging-guided therapy. *Sci. Robot.* **2**, eaaq1155 (2017).

12. Nelson, B. J., Kaliakatsos, I. K. & Abbott, J. J. Microrobots for minimally invasive medicine. *Annu. Rev. Biomed. Eng.* **12**, 55–85 (2010).
13. Osada, Y. & Rossi, D. D. *Polymer Sensors and Actuators* (Springer, 2013).
14. Noorduin, W. L., Grinthal, A., Mahadevan, L. & Aizenberg, J. Rationally designed complex, hierarchical microarchitectures. *Science* **340**, 832–837 (2013).
15. Lerch, M. M., Grinthal, A. & Aizenberg, J. Viewpoint: homeostasis as inspiration—toward interactive materials. *Adv. Mater.* **32**, 1905554 (2020).
16. Hippler, M. et al. Controlling the shape of 3D microstructures by temperature and light. *Nat. Commun.* **10**, 232 (2019).
17. Lahikainen, M., Zeng, H. & Priimagi, A. Design principles for non-reciprocal photomechanical actuation. *Soft Matter* **16**, 5951–5958 (2020).
18. Kim, Y., Yuk, H., Zhao, R., Chester, S. A. & Zhao, X. Printing ferromagnetic domains for untethered fast-transforming soft materials. *Nature* **558**, 274–279 (2018).
19. Kotikian, A., Truby, R. L., Boley, J. W., White, T. J. & Lewis, J. A. 3D printing of liquid crystal elastomeric actuators with spatially programmed nematic order. *Adv. Mater.* **30**, 1706164 (2018).
20. Lahikainen, M., Zeng, H. & Priimagi, A. Reconfigurable photoactuator through synergistic use of photochemical and photothermal effects. *Nat. Commun.* **9**, 4148 (2018).
21. Palagi, S. et al. Structured light enables biomimetic swimming and versatile locomotion of photoresponsive soft microrobots. *Nat. Mater.* **15**, 647–653 (2016).
22. Yan, Z. et al. Mechanical assembly of complex, 3D mesostructures from releasable multilayers of advanced materials. *Sci. Adv.* **2**, e1601014 (2016).
23. Zhang, H., Koens, L., Lauga, E., Mourran, A. & Möller, M. A light-driven microgel rotor. *Small* **15**, 1903379 (2019).
24. Zhang, Y. et al. Seamless multimaterial 3D liquid-crystalline elastomer actuators for next-generation entirely soft robots. *Sci. Adv.* **6**, eaay8606 (2020).
25. Qian, X. et al. Artificial phototropism for omnidirectional tracking and harvesting of light. *Nat. Nanotechnol.* **14**, 1048–1055 (2019).
26. Aizenberg, M., Okeyoshi, K. & Aizenberg, J. Inverting the swelling trends in modular self-oscillating gels crosslinked by redox-active metal bipyridine complexes. *Adv. Funct. Mater.* **28**, 1704205 (2018).
27. He, X. et al. Synthetic homeostatic materials with chemo-mechano-chemical self-regulation. *Nature* **487**, 214–218 (2012).
28. Gelebart, A. H. et al. Making waves in a photoactive polymer film. *Nature* **546**, 632–636 (2017).
29. Serak, S. et al. Liquid crystalline polymer cantilever oscillators fueled by light. *Soft Matter* **6**, 779–783 (2010).
30. Corbett, D. & Warner, M. Linear and nonlinear photoinduced deformations of cantilevers. *Phys. Rev. Lett.* **99**, 174302 (2007).
31. Corbett, D., Van Oosten, C. L. & Warner, M. Nonlinear dynamics of optical absorption of intense beams. *Phys. Rev. A* **78**, 013823 (2008).
32. White, T. J. & Broer, D. J. Programmable and adaptive mechanics with liquid crystal polymer networks and elastomers. *Nat. Mater.* **14**, 1087–1098 (2015).
33. Bisoyi, H. K. & Li, Q. Light-driven liquid crystalline materials: from photo-induced phase transitions and property modulations to applications. *Chem. Rev.* **116**, 15089–15166 (2016).
34. Buguin, A., Li, M. H., Silberzan, P., Ladoux, B. & Keller, P. Micro-actuators: when artificial muscles made of nematic liquid crystal elastomers meet soft lithography. *J. Am. Chem. Soc.* **128**, 1088–1089 (2006).
35. Yao, Y. et al. Multiresponsive polymeric microstructures with encoded predetermined and self-regulated deformability. *Proc. Natl. Acad. Sci. USA* **115**, 12950–12955 (2018).
36. Küpfer, J. & Finkelmann, H. Nematic liquid single crystal elastomers. *Makromol. Chem. Rapid Commun.* **12**, 717–726 (1991).
37. Liu, L. et al. Light tracking and light guiding fiber arrays by adjusting the location of photoresponsive azobenzene in liquid crystal networks. *Adv. Opt. Mater.* **8**, 2000732 (2020).
38. Lin, X., Saed, M. O. & Terentjev, E. M. Continuous spinning aligned liquid crystal elastomer fibers with a 3D printer setup. *Soft Matter* **17**, 5436–5443 (2021).
39. Ware, T. H., McConney, M. E., Wie, J. J., Tondiglia, V. P. & White, T. J. Voxelated liquid crystal elastomers. *Science* **347**, 982–984 (2015).
40. Pilz Da Cunha, M., Van Thoor, E. A. J., Debije, M. G., Broer, D. J. & Schenning, A. P. H. J. Unravelling the photothermal and photomechanical contributions to actuation of azobenzene-doped liquid crystal polymers in air and water. *J. Mater. Chem. C* **7**, 13502–13509 (2019).
41. Barrett, C. J., Mamiya, J. I., Yager, K. G. & Ikeda, T. Photo-mechanical effects in azobenzene-containing soft materials. *Soft Matter* **3**, 1249–1261 (2007).
42. Waters, J. T. et al. Twist again: dynamically and reversibly controllable chirality in liquid crystalline elastomer microposts. *Sci. Adv.* **6**, eaay5349 (2020).
43. Serra, F. & Terentjev, E. M. Effects of solvent viscosity and polarity on the isomerization of azobenzene. *Macromolecules* **41**, 981–986 (2008).
44. Erb, R. M., Sander, J. S., Grisch, R. & Studart, A. R. Self-shaping composites with programmable bioinspired microstructures. *Nat. Commun.* **4**, 1712 (2013).
45. Sydney Gladman, A., Matsumoto, E. A., Nuzzo, R. G., Mahadevan, L. & Lewis, J. A. Biomimetic 4D printing. *Nat. Mater.* **15**, 413–418 (2016).
46. Karothu, D. P. et al. The rise of the dynamic crystals. *J. Am. Chem. Soc.* **31**, 13256–13272 (2020).
47. Kaspar, C., Ravoo, B. J., van der Wiel, W. G., Wegner, S. V. & Pernice, W. H. P. The rise of intelligent matter. *Nature* **594**, 345–355 (2021).
48. Turiv, T. et al. Topology control of human fibroblast cells monolayer by liquid crystal elastomer. *Sci. Adv.* **6**, eaaz6485 (2020).
49. Hauser, A. W., Sundaram, S. & Hayward, R. C. Photothermocapillary oscillators. *Phys. Rev. Lett.* **121**, 158001 (2018).
50. Babu, D. et al. Acceleration of lipid reproduction by emergence of microscopic motion. *Nat. Commun.* **12**, 2959 (2021).

Publisher's note Springer Nature remains neutral with regard to jurisdictional claims in published maps and institutional affiliations.

© The Author(s), under exclusive licence to Springer Nature Limited 2022

Methods

Fabrication of LCE microstructures

The mixtures of liquid crystalline monomers, photoinitiator and azobenzene cross-linker were first made molten into the negative mould of the desired microstructures, covered with a coverslip and then slowly cooled to 60 °C. The mould with the prepolymer mixture was placed oriented in a weak magnetic field (approximately 0.5 T, NdFeB) to align the mesogens in an arbitrary direction relative to the microstructure principal axis. This molecular anisotropy was locked-in to the resulting LCE microstructures by UV polymerization, after which the sample was cooled down to room temperature and the mould was carefully peeled off.

Imaging of the LCE microstructure actuation

Microstructures were imaged by scanning electron microscopy. The thermal or photoactuation behaviour of LCE microstructures was studied by confocal fluorescence laser scanning microscopy, for which microstructures were stained with a Rhodamine B dye and imaged with 555 nm light focused on the top face of the microposts. For directional photoactuation with a 365 nm UV LED (Thorlabs M365F1), the microstructures were heated to 60 °C (above their glassy state, $T_g \approx 45$ °C) and deformation trajectories were followed as time series and by adjusting the focal plane as the posts deformed. The time series were subsequently image tracked using a MATLAB script. The scanning electron microscopy images of the deformed LCE microposts were obtained by ‘trapping’ the actuated shape in the glassy state of the LCE by rapidly cooling from 60 °C to room temperature.

Finite element simulations

Simulations were carried out using a custom finite element code written in C++, accounting for the energy of shear and bulk deformations of the elastomer, as well as a strain–nematic coupling proportional to the change in the order parameter, assumed to be proportional to the fraction of *cis*-isomers. At each time step, the isomerization at each mesh node was updated on the basis of the light intensity, computed by ray tracing through the finite element mesh and applying an attenuation derived from the isomerized fraction at that point in time.

Discrete model for arrays of microstructures

A simple discrete model was established to investigate the collective responses of arrays of microposts on directional irradiation. At each

time step, shadows created by the microposts were calculated and updated on the basis of the locations of the posts. The neighbouring shadows determine the illumination condition of each post, which in turn govern their deformation. The micropost array can therefore be modelled as a set of dynamic equations, which were solved by the Runge–Kutta method using MATLAB.

Data availability

The data supporting the findings of this study are included within the paper and its Supplementary Information files and are available from the corresponding author upon request.

Code availability

All codes needed to evaluate the conclusions in the paper are present in the paper and/or the Supplementary Information. Additional data related to this paper are available from the corresponding author upon request.

Acknowledgements This work was primarily supported by the US Army Research Office, under grant number W911NF-17-1-0351. K.B. and B.D. were supported by the National Science Foundation (NSF) through the Harvard University Materials Research Science and Engineering Center (MRSEC) under award DMR-2011754. M.M.L. was supported by the Netherlands Organization for Scientific Research (NWO, Rubicon Fellowship 019.182EN.027). Microfabrication and scanning electron microscopy were performed at the Center for Nanoscale Systems (CNS) at Harvard, a member of the National Nanotechnology Coordinated Infrastructure Network (NNCI), supported by the NSF ECCS award no. 1541959. We thank M. Aizenberg, M. Pilz Da Cunha, M. Liu, A. Chen and Y. Zhao for discussions.

Author contributions S.L., M.M.L. and J.A. conceived the project. S.L. and Y.Y. synthesized the side-on LCE monomer used for fabrication. S.L., M.M.L., R.S.M. and D.Y.K. performed the experiments. B.D. and K.B. performed theoretical modelling and image tracking. A.C.B. and J.T.W. performed finite element modelling. S.L., M.M.L., A.G., R.S.M. and B.D. analysed the experimental data. J.A. supervised the project. All co-authors provided useful feedback and contributed to the manuscript.

Competing interests The authors declare no competing interests.

Additional information

Supplementary information The online version contains supplementary material available at <https://doi.org/10.1038/s41586-022-04561-z>.

Correspondence and requests for materials should be addressed to Joanna Aizenberg.

Peer review information *Nature* thanks Peter Hesketh and the other, anonymous, reviewer(s) for their contribution to the peer review of this work.

Reprints and permissions information is available at <http://www.nature.com/reprints>.

Supplementary information

**Self-regulated non-reciprocal motions in
single-material microstructures**

In the format provided by the
authors and unedited

Supporting Information

Self-regulated non-reciprocal motions in single-material microstructures

Shucong Li^{#,1}, Michael M. Lerch^{#,2,3}, James T. Waters⁴, Bolei Deng², Reese S. Martens², Yuxing Yao¹, Do Yoon Kim², Katia Bertoldi², Alison Grinthal², Anna C. Balazs⁴, Joanna Aizenberg^{*,1,2}

¹ *Department of Chemistry and Chemical Biology, Harvard University, Cambridge, MA 02138;*

² *John A. Paulson School of Engineering and Applied Sciences, Harvard University, Cambridge, MA 02138;*

³ *Stratingh Institute for Chemistry, University of Groningen, Groningen, 9747 AG, The Netherlands*

⁴ *Chemical Engineering Department, University of Pittsburgh, Pittsburgh, PA 15261;*

[#] *Contributed equally*

Corresponding Author:

** jaiz@seas.harvard.edu*

This Supplementary Information includes:

Materials and Methods

Theoretical Models 1 to 3

Supplementary Results & Figures 1 to 35

Captions for Supplementary Videos 1 to 10

Further Supplementary Materials:

Supplementary Videos 1 to 10 (.mp4)

Table of Contents

1	MATERIALS AND METHODS	3
1.1	MATERIALS	3
1.2	METHODS	4
1.2.1	Materials Characterization	4
1.2.2	Image Tracking	5
1.2.3	Synthesis and Characterization of the Liquid Crystalline Elastomer (LCE) Monomer.....	5
1.2.4	Fabrication of LCE Microstructures.....	6
1.2.5	Fabrication of Freestanding Jointed LCE Microstructures	7
1.2.6	Comment on the mechanism of magnetic alignment.....	7
2	SUPPLEMENTARY MODELS	8
2.1	MODEL 1: FINITE ELEMENT SIMULATION.....	8
2.2	MODEL 2: THEORETICAL MODEL ¹² FOR NONLINEARITY IN ‘LIGHT-SEEKING’ AND ‘LIGHT-AVOIDING’ BEHAVIOR.....	10
2.3	MODEL 3: SIMPLIFIED DISCRETE MODEL FOR MICROPOST ARRAYS	11
3	SUPPLEMENTARY FIGURES	13
4	SUPPLEMENTARY VIDEOS	36
5	REFERENCES	38

1 Materials and Methods

1.1 Materials

General reagent information: For the preparation of commercially unavailable compounds, unless stated otherwise, all reactions were carried out in oven- and flame-dried glassware using standard Schlenk techniques and were run under argon atmosphere. The reaction progress was monitored by Thin-layer chromatography (TLC). Starting materials, reagents and solvents were purchased from *MilliporeSigma*, *Honeywell*, *J.T. Baker*, *Macron*, *Fischer*, or *Acros* and were used as received, unless stated otherwise. Solvents for the reactions were of quality puriss., p.a. Anhydrous solvents were purchased in septum-sealed bottles over molecular sieves. Deuterated solvents were purchased from *Cambridge Isotope Laboratories, Inc.* For aqueous solutions, deionized MilliQ water was used. 2,5-dihydroxybenzoic acid, benzyl bromide, 4-butyloxybenzoic acid, 4-hydroxybutyl acrylate, 4-pyrrolidinopyridine, *N,N'*-dicyclohexylcarbodiimide (DCC), fluorescein, palladium on carbon (10 w%, matrix activated), sodium bicarbonate (NaHCO₃), trichloro(1*H*,1*H*,2*H*,2*H*-perfluorooctyl) silane, and silica gel (Davisil Grade 633, high-purity grade, pore size 60 Å, 200-425 mesh particle size) were purchased from *MilliporeSigma*. Methacryloxyethyl thiocarbamoyl rhodamine B dye was purchased from *Polysciences, Inc.*

General considerations: Thin-layer chromatography analyses were performed on commercial Kieselgel 60 F₂₅₄ silica gel plates with fluorescence-indicator UV₂₅₄ (*Merck*, TLC silica gel 60 F₂₅₄). For detection of components, UV light at $\lambda = 254$ nm or $\lambda = 365$ nm was used. Alternatively, oxidative staining using aqueous basic potassium permanganate solution (KMnO₄), aqueous cerium phosphomolybdic acid solution (Seebach's stain¹), or iodine stain were used. Drying of solutions was performed with MgSO₄ and volatiles were removed with a rotary evaporator.

General analytical information: Nuclear Magnetic Resonance spectra were measured at the Harvard University Laukien-Purcell Instrumentation Center with a Varian Unity/Inova 500 spectrometer (500 MHz). All spectra were measured at room temperature (22–24 °C). Chemical shifts for ¹H-NMR spectra were reported relative to the residual solvent peak [in ppm; CDCl₃: $\delta_{\text{H}} = 7.26$]². The multiplicities of the signals are denoted by *s* (singlet), *d* (doublet), *t* (triplet), *q* (quartet), and *m* (multiplet).

Liquid crystalline elastomer constituents: Liquid crystal mesogen **1** was synthesized according to an established literature procedure³. The photoswitchable crosslinker (**2**, 4,4'-bis(9-acryloyloxynonyloxy) azobenzene) was purchased from *Synthon Chemicals* (ST04181). Photoinitiator IRGACURE[®] 819 (bis(2,4,6-trimethylbenzoyl)-phenylphosphineoxide) was purchased from *Ciba Specialty Chemical Inc.*

Microstructure fabrication: 4" Silicon wafers and 6" silicon-dioxide carriers were purchased from *Nova Electronic Materials*. Photoresist SPR220-7.0 was purchased from *Microchem*. Sylgard[®] 184 silicone kit was purchased from *Ellsworth Adhesive Systems* and used at a ratio 10:1 wt/wt Sylgard[®] base to curing agent. Cover glass (22 mm in diameter, 0.21 mm in thickness), microscopy glass slides (25 x 75 mm, 1 mm in thickness) and polyimide (Kapton[®]) tape were obtained from *VWR*. The high-temperature neodymium magnets (NdFeB, Grade N42SH; 1" x 1/2" x 1/2"; BX088SH) were purchased from *K&J Magnetics, Inc.* The magnetic field strength on the magnet was measured with a DC Gaussmeter (Model GM-1-ST) obtained from *AlphaLab Inc.*

UV-polymerization: A Dymax 2000-EC UV Curing Flood lamp with chamber (light intensity of ~18 mW/cm²) with a custom-made steel mesh (Gerard Daniel Worldwide, Inc., SST 304 TW, mesh .007, as neutral density filter) was used to initiate polymerization.

1.2 Methods

1.2.1 Materials Characterization

Differential Scanning Calorimetry (DSC) was performed on a Thermal Analysis (TA) DSC Q200 instrument. The program for monomer mixtures consisted of two cycles from $-5\text{ }^{\circ}\text{C}$ to $120\text{ }^{\circ}\text{C}$ and back with a $10\text{ }^{\circ}\text{C}/\text{min}$ rate. The program for the liquid crystalline elastomer consisted of two cycles from $-5\text{ }^{\circ}\text{C}$ to $200\text{ }^{\circ}\text{C}$ and back with a $10\text{ }^{\circ}\text{C}/\text{min}$ rate.

Scanning electron microscopy of the Si master and 'frozen' deformed LCE microstructures was performed on a Zeiss Supra55VP Field Emission Scanning Electron Microscope (FESEM). For experimental reasons, the SEM and the confocal images are not from exactly the same posts but from posts having the same director alignment.

Confocal Laser Scanning Microscopy (LSM) measurements were performed on a Zeiss LSM 700 instrument with 5X, 10X and 40X objectives and a custom-made sample holder to control the temperature across the LCE microstructured sample. For fluorescence read-out, LCE microstructures were coated with a solution of the dye methacryloxyethyl thiocarbamoyl rhodamine B in ethanol, that was applied dropwise to the sample and left evaporating. The fluorescent dye was excited with a $\lambda_{\text{ex}} = 555\text{ nm}$ laser during measurements. For directional photoactuation with a 365 nm UV LED (Thorlabs M365F1), the microstructures were heated to $60\text{ }^{\circ}\text{C}$ (above their glassy state, $T_g \sim 45\text{ }^{\circ}\text{C}$) and deformation trajectories were followed as time-series and by adjusting the focal plane as the posts deformed. The time-series were subsequently image-tracked using a MATLAB script. Confocal images of *i/iv* and *ii/iii* in Manuscript Figure 2 were taken from two different microposts having the same director alignment. For water-immersion, fluorescein dye (excited with $\lambda_{\text{ex}} = 488\text{ nm}$) was used. Z-stack and time series data were analyzed with the Zeiss ZEN black software.

For UV-irradiations, an LED mounted in a heatsink (Thorlabs, M365F1) was used and controlled with a T-cube driver (Thorlabs, LEDD1B) for continuous adjustment of light-intensity. Twelve levels of intensity were used: (1) $1.0\text{ mW}/\text{cm}^2$, (2) $2.5\text{ mW}/\text{cm}^2$, (3) $4.8\text{ mW}/\text{cm}^2$, (4) $9.0\text{ mW}/\text{cm}^2$, (5) $12.6\text{ mW}/\text{cm}^2$, (6) $15.8\text{ mW}/\text{cm}^2$, (7) $24.8\text{ mW}/\text{cm}^2$, (8) $42.1\text{ mW}/\text{cm}^2$, (9) $66.2\text{ mW}/\text{cm}^2$, (10) $90.0\text{ mW}/\text{cm}^2$, (11) $103.8\text{ mW}/\text{cm}^2$, and (12) $115.0\text{ mW}/\text{cm}^2$. Irradiance levels were determined at 1 cm distance from the light-source with a power meter (Thorlabs, S310C in conjunction with PM100D). For irradiation in intervals, a Transistor Transistor Logic (TTL) signal provided by an Arduino Uno controller was used to switch on or off the LED through the Trigger Mode of the T-cube driver.

UV-visible spectra were obtained on an Agilent 8453 UV-vis diode array spectrophotometer equipped with a Peltier-based temperature-controlled cuvette holder. Samples were prepared with Uvasol[®]-grade solvents and measured in quartz cuvettes of 10 mm pathlength. The obtained UV/vis spectra were baseline corrected. Data-analysis was performed using R (<https://www.r-project.org/>), GraphPad Prism, or Spectragryph software. Photoswitching of crosslinker **2** in dichloromethane solution was performed with an LED M365F1 (Thorlabs) at room temperature. Spectra for photoswitching within a polymeric thin film (non-aligned LCE, with 7.5 wt% compound **2** as crosslinkers) were collected at $60\text{ }^{\circ}\text{C}$ by immersing the polymer film in quartz cuvettes filled with water upon irradiation with LED M365FP1 (Thorlabs).

To monitor photothermal heating, a thermal IR camera (FLIR, A8303sc, InSb detector, 3.0–5.0 μm spectral range, 1280x720 resolution, f/4.0, GigE/CXP 60Hz) with a 4X microscope lens objective (FLIR, 50 mm lens) was used. Time-series were analyzed with ResearchIR software. The IR camera was placed on a boom tripod and suspended above the sample for imaging. The

sample was placed on a heating element at 60 °C on a lab jack (Thorlabs, L490) for focus adjustment.

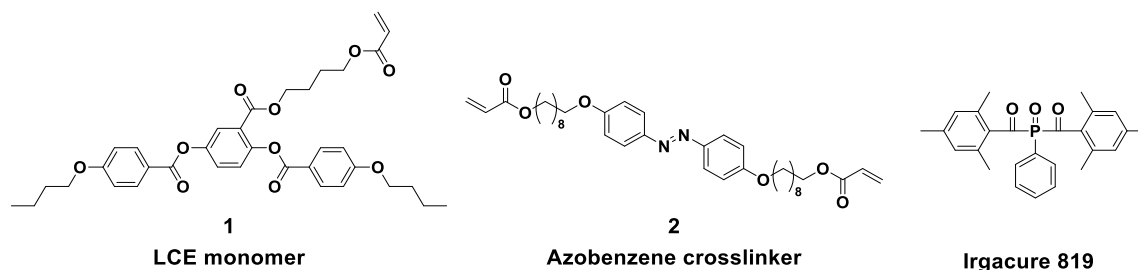
1.2.2 Image Tracking

The positions and rotations of the LCE microposts were tracked based on experimental videos by fluorescent confocal microscopy using MATLAB (Supplementary Figure 12). The image tracking process takes three steps in MATLAB:

- (1) Experimental videos were converted to image sequences, where each frame corresponds to an image;
- (2) For each image, a color threshold was first set to convert the image into a binary plot, where the pixels inside the post have a value of 1 and pixels outside the post have a value of 0. Then the boundary of the considered micropost was extracted for each binary figure using the MATLAB function 'bwboundaries';
- (3) Finally, the boundary of the micropost was fit by a square using linear regression, in which the residue function is defined by the summation of distances between the post boundary and the fitting square. The fitted square contains information about the position and rotation of the micropost at every time point.

1.2.3 Synthesis and Characterization of the Liquid Crystalline Elastomer (LCE) Monomer

Synthesis: Following a previously published procedure by Ratna and co-workers³, side-on LC monomer **1** ((4"-acryloyloxybutyl) 2,5-di(4'-butyloxybenzoyloxy)benzoate) was synthesized in four steps from commercially available starting materials (Supplementary Figure 2). Spectral properties matched previously reported values: ¹H-NMR (500 MHz, CDCl₃) δ (ppm): 1.00 (*t*, *J* = 7.4, 2.6 Hz, 6H), 1.46–1.68 (m, 8H), 1.75–1.86 (m, 4H), 3.95–4.09 (m, 6H), 4.20 (*t*, *J* = 6.0 Hz, 2H), 5.77–5.82 (m, 1H), 6.03–6.12 (m, 1H), 6.32–6.40 (m, 1H), 6.92–7.02 (m, 4H), 7.26–7.28 (m, 1H), 7.43–7.48 (m, 1H), 7.89 (s, 1H), 8.10–8.19 (m, 4H).



Preparation of LC monomer mixture: 90.5 mg of side-on monomer **1**, 7.5 mg of photoresponsive crosslinker **2**, and 2 mg of IRGACURE[®] 819 were dissolved in roughly 0.5–1 mL of anhydrous dichloromethane in a vial, mixed thoroughly, and applied dropwise to a cleaned microscopy glass slide (washed sequentially with water, acetone, and 2-propanol, then blow-dried under nitrogen flow). The solvent was allowed to slowly evaporate overnight in the dark to yield the crystallized LC monomer mixture. The amounts correspond to 7.7 mol% (crosslinker **2**) and 3.0 mol% (photoinitiator). The crystallized LC monomer mixture on the glass slide can be conveniently scratched off onto the hot PDMS mold during the next fabrication step.

1.2.4 Fabrication of LCE Microstructures

Fabrication of the microstructured silicon master: The microstructured silicon master was produced by photolithography followed by reactive ion etching (RIE) at the Center for Nanoscale Systems (CNS) at Harvard University. Photoresist (SPR220-7.0) patterning was performed by UV exposure at 375 nm (470 mJ/cm^2) with a Heidelberg MLA150 Maskless Aligner, held overnight (or at least for 2 h), and developed in CD-26 developer (2 min x 2 times, MICROPOST[®] MF[®]), which later served as the mask for the anisotropic etching of the Si wafer substrate using the SPTS Technologies Rapier DRIE System (Model Omega LPX Rapier), to obtain the array of Si microstructures. The geometry and size of the structures fabricated for this study are shown in Supplementary Figure 1. For a height of $150 \mu\text{m}$ two rounds of subsequent etching runs ($2 \times 75 \mu\text{m}$) were required. The 3D structure of the Si microposts was characterized by scanning electron microscopy (Zeiss Supra 55 VP Field Emission Scanning Electron Microscope, FESEM).

Fabrication of the molds for LCE microstructures^{4,5}: After removal of the remaining photoresist with oxygen plasma (PlasmaEtch, PE-200, 300W, 20 min), the Si microstructure array was functionalized with trichloro(1*H*,1*H*,2*H*,2*H*-perfluorooctyl) silane to render the microstructures hydrophobic. Subsequently, a PDMS negative replica of the microstructured surface was generated by pouring the well-mixed (using a Thinky Mixer ARE-310, Thinky U.S.A., Inc.) polydimethylsiloxane (PDMS) precursor (mixture of Sylgard[®] 184 base and crosslinker at a ratio of 10:1 *wt:wt*) on top of the Si wafer, degassing and curing at $70 \text{ }^\circ\text{C}$ for 2 h. Finally, the PDMS was carefully peeled off from the Si wafer and used as a negative mold for the synthesis of LCE microstructures.

Synthesis of LCE microstructures: The crystallized monomer mixture ($\sim 20 \text{ mg}$) was scratched from the prepared glass slide onto the PDMS mold and molten into molding cavities. The mold was then covered with a microscopy glass coverslip (held in place by Kapton[®]-tape) and placed oriented in a magnetic field generated by the desired geometric assembly of NdFeB-based magnets with a surface field of approximately 0.5 T to align the LC mesogens in an arbitrary direction relative to the microstructures' principal axes (Supplementary Figure 3a). When the sample had reached $80 \text{ }^\circ\text{C}$ (isotropic phase), the setup was slowly cooled down to $60 \text{ }^\circ\text{C}$ at a rate of $1 \text{ }^\circ\text{C/min}$, and then polymerized under UV irradiation (Dymax 2000-EC UV Curing Flood Lamp System with a custom metal mesh reducing light intensity to $\sim 18 \text{ mW/cm}^2$)⁵ under inert atmosphere (N_2) for 1 h. To keep the azobenzene moiety from photoisomerizing (disruption of alignment) and possible photodegradation during UV-polymerization, an optical cut-off filter (Newport FSQ-GG400) was used, that blocks any light with wavelength shorter than 400 nm. After $\sim 1 \text{ h}$ of polymerization, the sample with the encrypted nematic director orientation was cooled down to room temperature and the PDMS mold was carefully peeled off from the LCE microstructures on the glass coverslip.

Synthesis of the LCE thin film for UV-Visible measurements: We applied $\sim 10 \text{ mg}$ of the reactive monomer mixture onto a flat rectangular PDMS slab on a hot plate at $80 \text{ }^\circ\text{C}$ (isotropic phase) and placed two $6 \mu\text{m}$ plastic spacers at the two ends of the PDMS slab. We then covered the molten mixtures with a microscopy glass coverslip (held in place by Kapton[®]-tape). Cooling and polymerization of the thin film were conducted under the same conditions as for the LCE microstructure described above. After $\sim 1 \text{ h}$ of polymerization, the sample was cooled down to room temperature and the PDMS mold and spacers were carefully removed leaving the thin film attached on the coverslip. The coverslip was later cut into a narrow piece to be able to fit into the quartz cuvettes of 10 mm path length for the UV-Vis measurements.

1.2.5 Fabrication of Freestanding Jointed LCE Microstructures

Freestanding jointed LCE microstructures (V- and X-shape) were synthesized following a procedure resembling the one described in SI section 1.2.4 (Supplementary Figure 32). Instead of a glass coverslip, however, a thin PDMS slab was used as cover to avoid surface attachment (less adhesion) of the polymerized LCE structure. After placing the flat PDMS slab onto the negative PDMS mold filled with the LC mixture melt, gentle pressure was applied to enhance contact between the two PDMS layers as well as to remove any excess LC mixture. In addition, a trace amount of oxygen (from air) in the PDMS mold helps to suppress polymerization at the PDMS-PDMS interface and therefore to avoid formation of a thin LCE layer in between. The same magnet, alignment, and polymerization setup as described in SI section 1.2.4 (Supplementary Figure 3a) were used to yield polymerized LCE microstructures with jointed shape. Upon polymerization, stretching and squeezing the flexible PDMS mold helps to release the LCE microstructure. Custom-made capillary tubes (the thin end has a diameter of ~10 μm) were used to pick up the released freestanding LCE microstructures and fix certain spots for further UV actuation and microscopy imaging. Note that for structures in which a thin LCE layer remains, this thin substrate layer could in principle also (undesirably) influence the overall jointed microstructure deformation. The described procedure avoids formation of such a film as much as possible.

1.2.6 Comment on the mechanism of magnetic alignment

The propensity of monomer **1** ((4"-acryloyloxybutyl) 2,5-di(4'-butyloxybenzoyloxy)benzoate), a type of calamitic LC mesogen, to align within a magnetic field is well-established^{3,7,8}. Calamitic LCs are often diamagnetic due to a zero-net spin and the dispersed electron distribution associated with the delocalized charge, for example, from phenyl rings in the mesogen structure. When placed in a magnetic field, the ring currents associated with these aromatic units induce a magnetic moment perpendicular to the conjugated aromatic ring plane in opposition to the applied magnetic field, which thereby raises the free energy. The density of free energy g_{mag} in LC mesogens in a magnetic field can be expressed as⁹:

$$g_{mag} = g_0 - \frac{1}{2}\mu_0^{-1}B^2\chi_{\perp} - \frac{1}{2}\mu_0^{-1}\Delta\chi(\mathbf{B} \cdot \mathbf{n})^2$$

where $\Delta\chi = \chi_{\parallel} - \chi_{\perp}$, with χ_{\parallel} and χ_{\perp} being the magnetic susceptibilities parallel and perpendicular to the LC mesogen principal axis, respectively. μ_0 denotes the permeability of free space, and \mathbf{B} refers to the magnetic field and \mathbf{n} is the director. For most calamitic LCs, both χ_{\parallel} and χ_{\perp} are negative but the delocalized electron density makes a major contribution to χ_{\perp} resulting in $|\chi_{\perp}| > |\chi_{\parallel}|$ and $\Delta\chi$ positive. Therefore, in order to minimize the free energy, the director \mathbf{n} will align parallel to the magnetic field \mathbf{B} ⁹ (Supplementary Figure 3b). In our research, we use an externally applied weak magnetic field (~0.5 T) to orient mesogens uniaxially within the molded LCE precursor mixture in an arbitrary direction in 3D by simply changing the orientation of the mold within the static magnetic field. Polymerization locks in this uniaxial nematic director orientation within the resulting microstructures. (Note that magnetic field is only used during the fabrication and not in subsequent actuation process.)

2 Supplementary Models

2.1 Model 1: Finite Element Simulation

To obtain a detailed description of the evolution of the shape deformation, twisting, and deflection of the post, and how these properties relate to the propagating isomerization front, we implemented a finite element model to simulate the behavior of the micropost in response to light at different intensities and illumination directions, for different orientations of the nematic director.

The material is discretized into a set of hexahedral (initially cubic) finite elements, each bounded by eight nodes. The evolution of the mesh in time is dictated by the free energy of the system, summed over all of the finite elements constituting the post. This free energy can be differentiated with respect to the nodal coordinates to update the dynamics of the system at each time step^{6,10}. This free energy is given as

$$F = \frac{\kappa}{2} \log^2 J - \frac{\mu(I_m-3)}{2} \log\left(\frac{I_m-I_1}{I_m-3}\right) + \alpha \Delta S Q_{ij} \epsilon_{ij} \quad (\text{S1})$$

where the first and second terms describe the resistance of the material to bulk and shear deformations, respectively. κ is the bulk modulus of the material, taken to be 28 MPa, and μ is the shear modulus, taken to be 570 KPa, as used in earlier numerical studies^{6,10}. I_1 and J are the first invariant and square root of the third invariant of the strain tensor ϵ_{ij} , and I_m is a limiting extension of polymer chains within the material, here taken to be 30. The third term describes the tendency of the material to deform brought on by changes in the polymer chain conformations as the system moves from the nematic to the isotropic state. In this term, the coupling coefficient α was fit as 0.175μ in a prior study^{6,10}. Q_{ij} is the traceless nematic tensor, assumed to be fixed in the frame of the material.

In our numerical model, the change in nematic order ΔS in this third term is negative and assumed to be proportional to the fraction of the azobenzenes in the *cis*-state. Using the theoretical model of Warner and co-workers¹¹, the isomerization of the photoswitches in the material is evolved in time at each location in the mesh, as a function of the incident light intensity:

$$\frac{\partial n_t}{\partial t} = -\Gamma I n_t + (1 - n_t)/\tau . \quad (\text{S2})$$

Here n_t represents the fraction of the system in the *trans*-state, which must sum to one with the *cis*-fraction n_c .

The first term on the right-hand side in the above equation corresponds to the excitation of *trans*-isomers, and depends on the fraction of remaining *trans*-isomers and the incident light intensity I . The constant Γ determines the *trans*-to-*cis* transition rate and chosen to have a value of $10^{-5} \text{ s}^2/\text{Kg}$ to match the experimentally observed response at low and high intensities. The second term describes the relaxation of *cis*-isomers back to the *trans*-state which is dictated by a relaxation time τ , here taken to be 120 s, corresponding to the experimentally observed timescale of minutes. This time evolution is solved at each node in the mesh at each time step of the simulation. To obtain the incident light intensity, we perform a ray-tracing algorithm through the elements of the mesh to each node. An attenuation length λ_j is calculated for each element j , based on the isomerized fraction n_t at each node i comprising the element:

$$\lambda_j = \frac{\gamma \Gamma}{8} \sum_{i=1}^8 n_t^i . \quad (\text{S3})$$

The constant γ , representing the number density of chromophores and the energy of each transition, is set to a value of $2 \times 10^{10} \text{ Kg/ms}^2$ to reproduce the appropriate Beer length ($l_B = 1/\gamma\Gamma = 5 \mu\text{m}$) at low intensities. For light incident along a vector \hat{v}_l and a mesh node i located at \mathbf{r}_i , we can check each of the elements containing node i for a face consisting of four points \mathbf{r}_j ($j = 1,2,3,4$) such that a ray parallel to \hat{v}_l intersecting the face can reach \mathbf{r}_i . This is equivalent to solving the equation

$$\mathbf{r}_i = l_B \hat{v}_l + \sum_{j=1}^4 \alpha_j \mathbf{r}_j \quad (\text{S4})$$

where the α_j coefficients are the finite element shape functions evaluated on the face of the element. These coefficients are nonnegative and sum to unity, and the path length l_B must be greater than zero. The value of these shape functions at the point of intersection will give us the weights to assign to each of the intensities when relating them to the intensity at the point of interest. The quantity l_B is the path length through the element to the node i along the incident light vector, allowing us to write the intensity at \mathbf{r}_i as a function of these quantities, the intensity at other nodes, and the local attenuation length λ for the element in question:

$$I_i = e^{-\lambda l_B} \sum_{j=1}^4 \alpha_j I_j . \quad (\text{S5})$$

Mesh nodes that lie on a surface of the post directly exposed to the light will be assigned an intensity I_0 , equal to that at the light source. Additional relations of the same form as S5 may be necessary if there are nodes and faces satisfying equation S4 but belonging to different elements—such a case would correspond to light passing through the material for some distance, passing outside the material, and then striking the surface of the post again, and is possible if the post deforms into a nonconvex shape. In this instance, the attenuation per length of light outside of the micropost is assumed to be negligible.

This will give a system of linear equations that can then be solved to obtain the intensity at each node in the finite element mesh. This is used to update the isomerized fraction, which in turn is used to update the accelerations of the mesh nodes and the attenuation length through each mesh element, which will be used to compute the intensities for subsequent time steps.

The above methodology can then be extended to arrays of posts, with equation S4 used to trace light rays through one structure and into another disconnected structure and determine what parts of the surface of each post will be obscured by neighboring posts. Such simulations predict interactions within arrays of posts similar to what was observed experimentally (Supplementary Figure 27, Video 6). We find that for a row of posts, we can approximate the effect of a finite-size light source in experiment with two ideal light sources (assumed to be propagating from infinity along all vectors parallel to \hat{v}_l) separated at an angle of $\pm 1^\circ$ from the post-to-post separation axis. The first post on the path of the incident light bends towards the light as it would in isolation. However, the second post is subject only to glancing incidence on its sides—it is unstable in the sense that a slight deflection out of the plane defined by the vertical axes of the posts and the line connecting the post bases will lead to more isomerization on that face. This will induce more contraction and further deflection out of the plane. The direction of this out-of-plane deflection of the second post will cause selective irradiation of the next (third) post from any glancing incidence but not the other. This causes the third post in the sequence to deflect out of plane in the opposite direction. This out-of-plane deflection will in turn change irradiation of the subsequent post, and the effect will propagate along the line of posts.

2.2 Model 2: Theoretical Model¹² for Nonlinearity in ‘Light-seeking’ and ‘Light-avoiding’ Behavior

Let us consider the LCE molecules with the director θ away from Z axis in the YZ plane. When actuated, the molecular alignment induces a contraction with a strain $-\varepsilon_a$ along the LCE director. Furthermore, due to the Poisson effect (as the material keeps constant volume), the material expands perpendicular to its alignment by $\varepsilon_a/2$ (Supplementary Figure 15a). To facilitate our analysis, we decompose the strain state in the Y-Z axes and represent the strain state by normal strain ε_{yy} , ε_{zz} and shear strain τ_{yz} (Supplementary Figure 15a):

$$\begin{aligned}\varepsilon_{yy} &= -\frac{\varepsilon_a}{4} + \frac{3\varepsilon_a}{4} \cos(2\theta) \\ \varepsilon_{zz} &= -\frac{\varepsilon_a}{4} - \frac{3\varepsilon_a}{4} \cos(2\theta) \\ \tau_{yz} &= \frac{3\varepsilon_a}{4} \sin(2\theta) .\end{aligned}\quad (\text{S6})$$

For the studied micropost, we denote its height as h and edge length as a . As the UV light activates the material only within the thickness l_B (penetration depth), the activated part deforms with the strain state described by ε_{yy} , ε_{zz} and τ_{yz} . Such deformation can be approximated as two separate parts, a shear component with strain τ_{yz} and a shortening component in Z-direction with strain ε_{zz} (Supplementary Figure 15b), resulting in shearing and bending deformation modes, respectively. Note that any deformation in Y-direction is assumed to have no effect on the final configuration of the post. The total deformation of the micropost can be calculated as the sum of these two deformation modes (Supplementary Figure 15c), *i.e.*, (i) shearing and (ii) bending due to the shortening of the activated part.

- (i) For the shear deformation, the total tip displacement can be approximated by

$$y_1 = \tau_{yz} \frac{d}{a} h = \frac{3hl_B\varepsilon_a}{4a} \sin(2\theta). \quad (\text{S7})$$

- (ii) The bending deformation part is much more complex. As we combine the shortened ‘activated’ part (shortened by $\Delta h = \varepsilon_{zz}h$) with the original part, due to the mismatch between the two parts, the final configuration bends. Furthermore, due to the interaction between the two parts, both parts not only bend but also stretch/compress axially. We set the length of the ‘activated’ part to h_1 and the ‘passive’ part to h_2 . The balance of force in the axial direction gives,

$$F = Ea(a - l_B) \frac{h-h_2}{h} = Eal_B \frac{h_1-h+\Delta h}{h}. \quad (\text{S8})$$

The compatible requirement between the bending and elongation of the beams gives geometrical constraint

$$\frac{a}{2}\beta = h_2 - h_1 \quad (\text{S9})$$

where β is the radian of the bent beam. The moment generated by the eccentric forces inside each beam should balance the moment due to the bending of the beams. Therefore,

$$F \frac{a}{2} = \frac{EI\beta}{h} \quad (\text{S10})$$

where $I = \frac{1}{12} a^4$ is the moment of inertia of the beam cross-section. Combining equations S8–S10, one can solve for h_1 and h_2 , giving

$$h_1 = h - \Delta h + \frac{\Delta h}{\frac{h}{h-\Delta h} \left(\frac{6l_B}{a} + \frac{l_B}{a-l_B} \right) + 1}, \text{ and } h_2 = \frac{ah-d(h_1+\Delta h)}{a-l_B}. \quad (\text{S11})$$

The distance traveled by the tip due to this deformation mode is expressed as

$$y_2 = \frac{h\beta}{2} = \frac{h(h_2-h_1)}{a}. \quad (\text{S12})$$

The total distance travelled by the post top is then the combined contribution of both deformation modes

$$y = y_1 \pm y_2. \quad (\text{S13})$$

For the ‘light seeking’ case, equation S13 takes “+” sign; for the light avoiding case, equation S13 takes “-” sign.

In Supplementary Figure 16 we plot the distance traveled by the post top y as a function of penetration depth l_B for both light seeking and light avoiding cases with different post edge length a and director angle θ .

2.3 Model 3: Simplified Discrete Model for Micropost Arrays

To capture the collective response of a micropost array to irradiation, we establish a simple discrete model. We consider an array of cylindrical posts with diameter a that are exposed to UV light forming an angle β with Y-axis. Because the spot size of the UV light is comparable to its distance from the micropost array, we assume that the shadow formed by a cylindrical post has a long triangular shape and is characterized by its length L_{shadow} (Supplementary Figure 26a). Note that L_{shadow} depends on many factors, for instance, the distance, spot size and collimation of the UV light, therefore in our model we treat L_{shadow} as a fitting parameter to part of the experimental measurements.

When the array of microposts is exposed to UV light, every microstructure generates a triangular shadow whose direction is determined by light angle β . For each post, we can loop over all other posts to figure out which part of the microstructure is being shadowed by others. For the parts that are not being shadowed, the UV light penetrates l_B into the post and activates certain areas of the post (Supplementary Figure 26b). Note that since the microposts considered in our study have a thin skin layer that does not respond to UV light, in our model the outer ring with thickness δ_{non} is also not activated. To model the equivalent bending force generated by the illuminated areas S_{light} , we introduce a local coordinate x' and y' that is aligned with the light direction. The equivalent force on the post is therefore calculated as

$$F_{light}^{x'} = \int_{S_{light}} P_{light} x' dS_{light} \quad (\text{S14})$$

$$F_{light}^{y'} = \int_{S_{light}} P_{light} y' dS_{light} \quad (\text{S15})$$

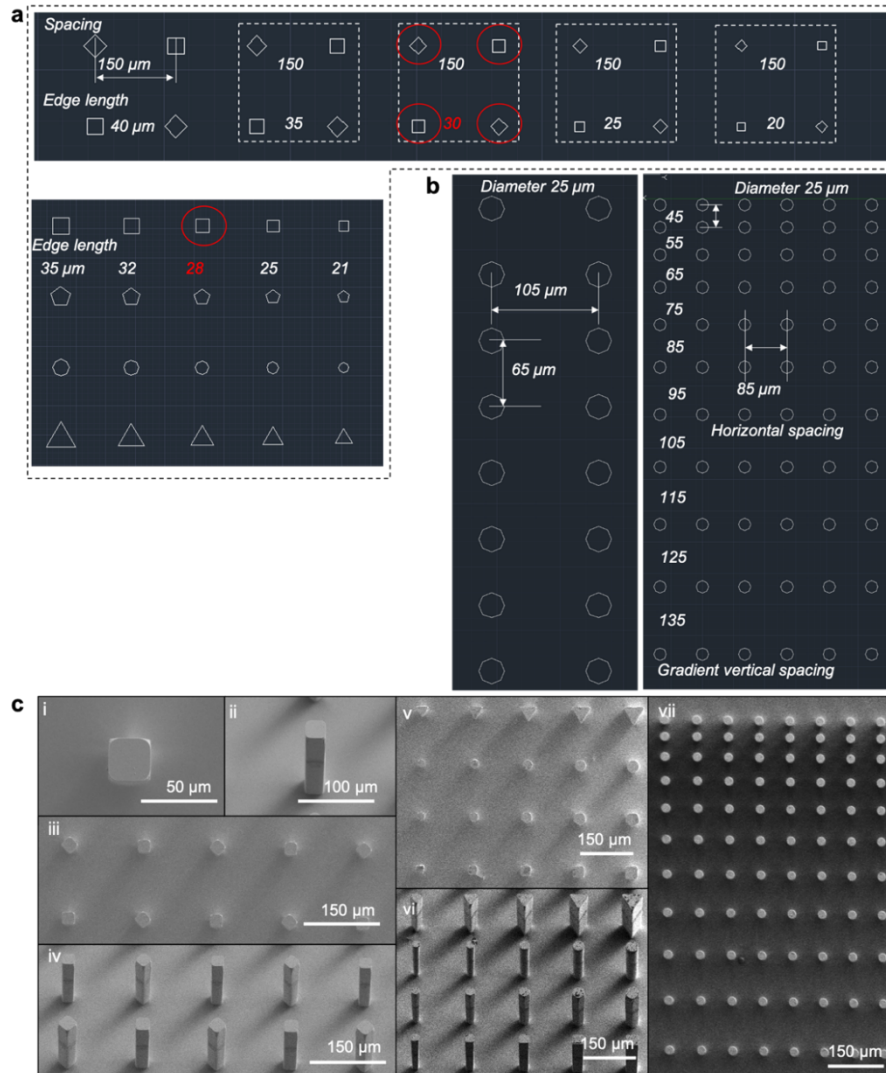
where P_{light} is another fitting parameter characterizing how strong the posts respond to the UV light. For the sake of simplicity, we use the vector \vec{F}_{light} to denote this force.

Furthermore, since the microposts are 3D objects, their shadows are also in 3D. To address this point, we discretize the post as a stack of N disks (Supplementary Figure **26c**). We simply assume that upon activation the post deforms linearly as a tilted straight line. Then the light-induced force is calculated depending on the positions of posts at each layer i , as \vec{F}_{light}^i . Compared to the disks on the top, disks near the bottom have a larger effect on the positions of the post tip. Therefore, the total equivalent force is defined as $\vec{F}_{light}^{total} = \frac{1}{N} \sum_{i=1}^N \frac{N-i-1}{N} \vec{F}_{light}^i$. Finally, we use two linear springs k_x and k_y to model the elastic resistance of the posts during bending (Supplementary Figure **26d**). The balance between the light-induced force and the linear springs yields the final positions of the post tips,

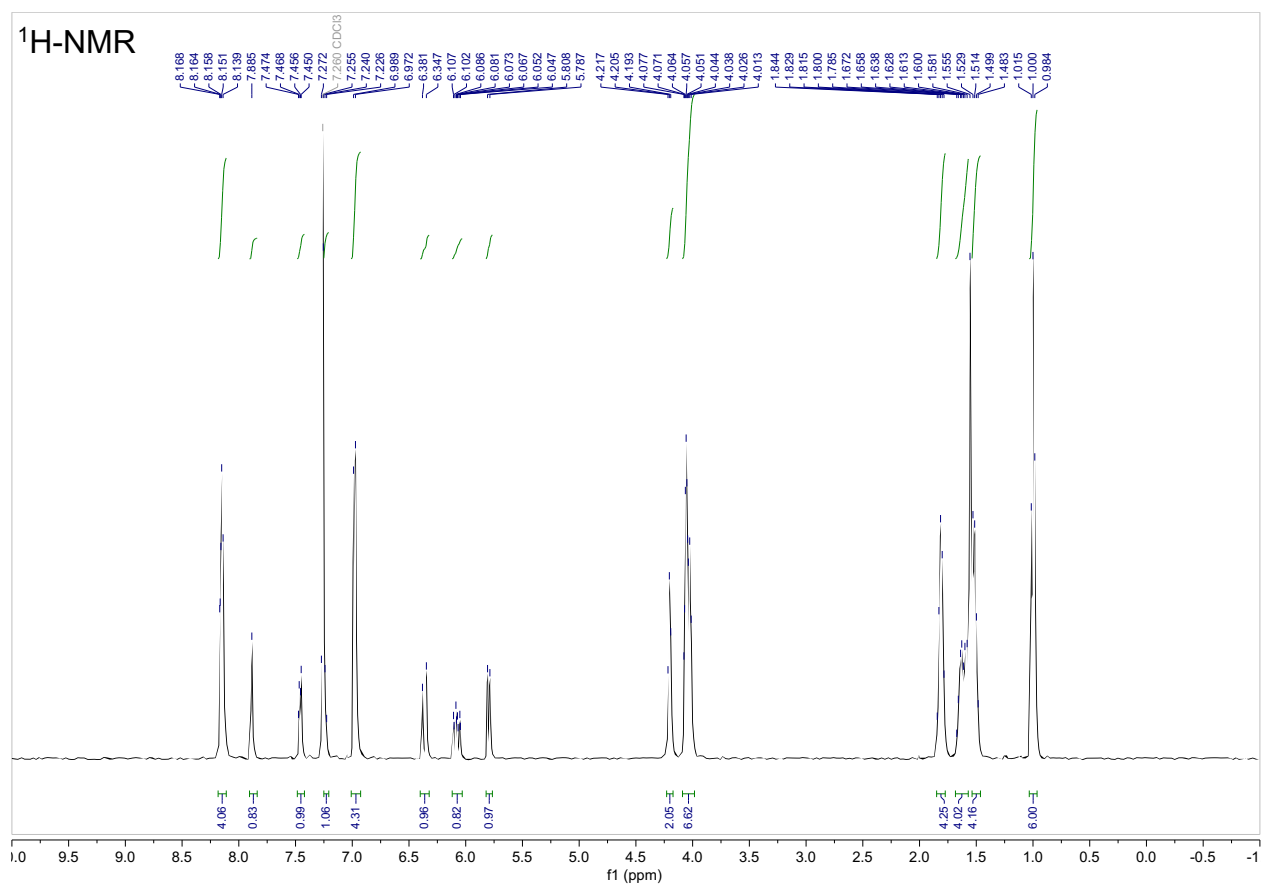
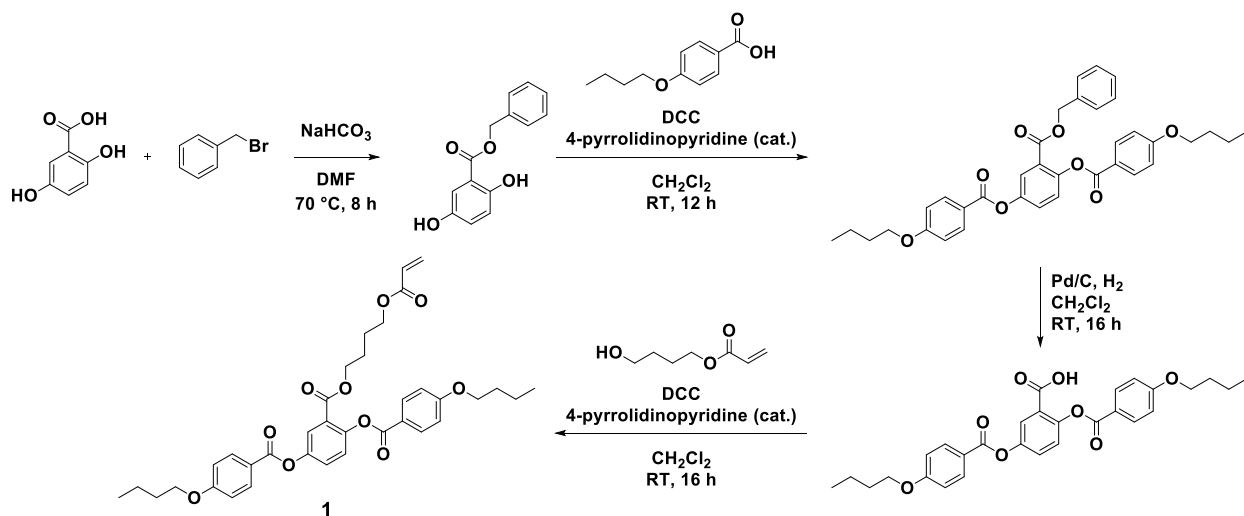
$$k_x u = \vec{F}_{light,x}^{total} \text{ and } k_y v = \vec{F}_{light,y}^{total} \quad (\text{S16})$$

where u and v are the x and y -displacements of the post tip. Equation S16 is solved numerically for different post distributions and light directions using the Runge-Kutta method with MATLAB.

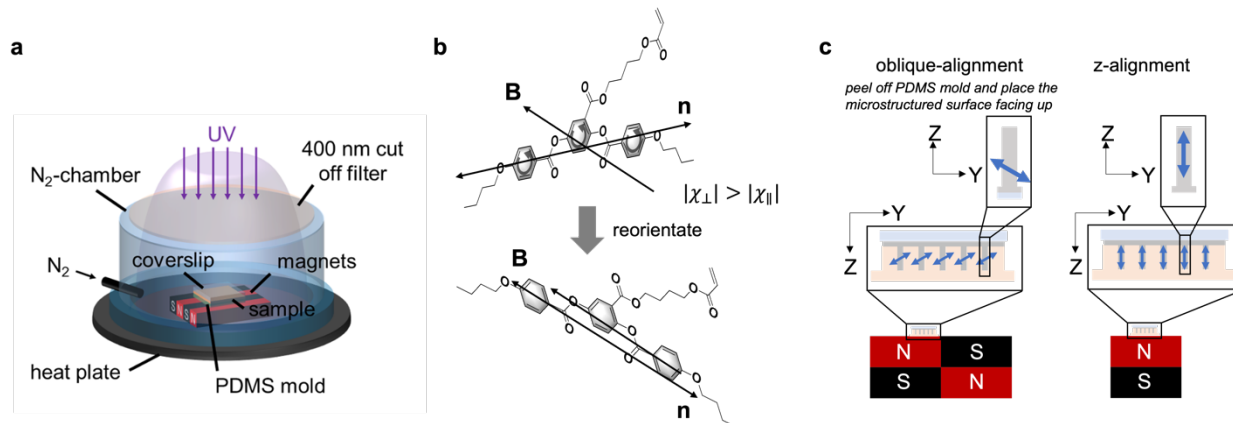
3 Supplementary Figures



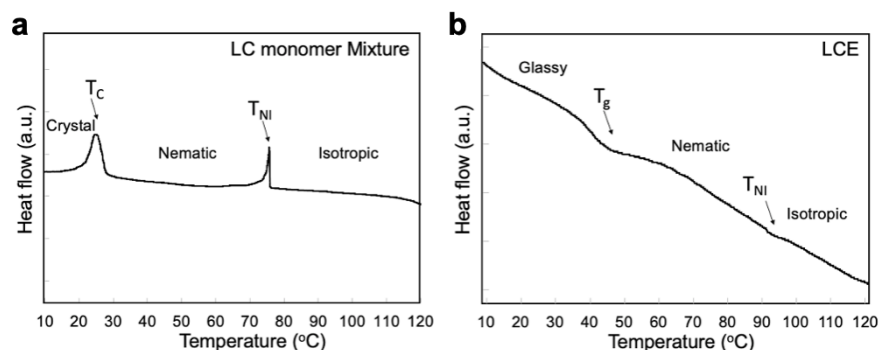
Supplementary Figure 1 | **a.** Depiction of AutoCAD files used for photolithography on Si wafers. Note the two existing surface designs: one comprising a square/diamond pattern and one including multiple geometries (squares, pentagons, circles, and triangles). Both designs include a gradual change of edge lengths to explore the influence of micropost dimensions on bending/flexural stiffness and deformation behavior. A constant interpost spacing of $150\ \mu\text{m}$ was chosen across the array to avoid potential shadowing from neighbors. Squares with an edge length of $28\ \mu\text{m}$ and $30\ \mu\text{m}$ (red circles) were found to represent a good compromise between mechanical flexibility and quality of magnetic alignment. Square geometry allows for clear visual identification of distinct deformations linked to different illuminated faces of the micropost. **b.** Furthermore, we designed closely packed multipost arrays with uniform (left) or gradient (right) interpost spacing to study post communication effects for collective deformation pattern formation. **c.** Close-up field emission scanning electron microscopy (FESEM, Zeiss Supra 55 VP) images of Si microstructures: a single square micropost of $30\ \mu\text{m}$ side length (i) top- and (ii) sideview; the square/diamond pattern (iii) top- and (iv) side-view; the multiple geometry design (v) top- and (vi) sideview; and (vii) the top-view of the multipost array with gradient interpost spacing. All microstructures are $150\ \mu\text{m}$ in height (calculated from the SEM tilted-view image).



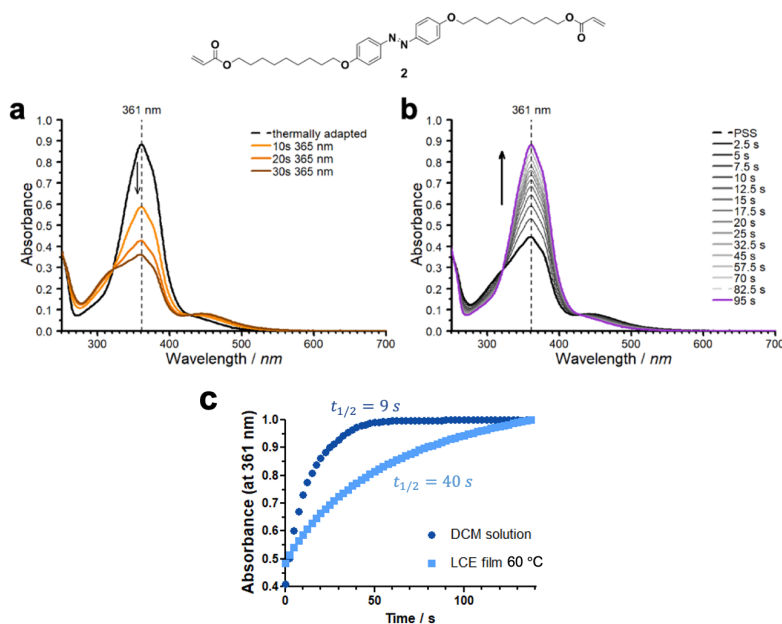
Supplementary Figure 2 | Literature-based synthetic route³ to side-on liquid crystalline (LC) monomer **1** ((4''-acryloyloxybutyl) 2,5-di(4'-butyloxybenzoyloxy)benzoate). For details on the synthesis, please refer to SI section 1.2.3. The ¹H-NMR spectrum of compound **1** in deuterated chloroform is included. Please also refer to our previously reported work⁶.



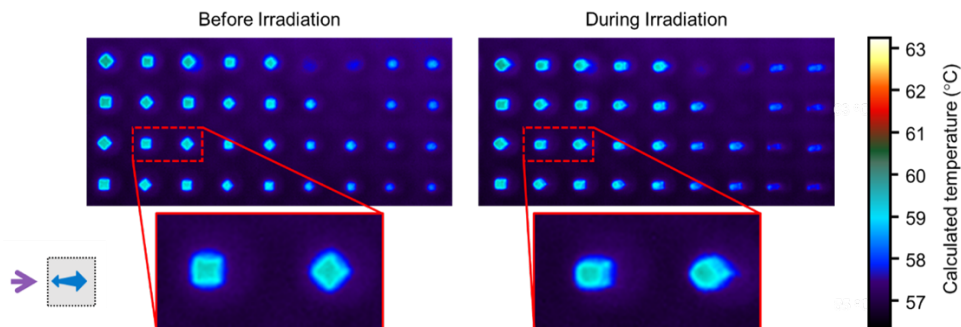
Supplementary Figure 3 | a. Schematic depiction of the experimental setup for the synthesis of microstructured LCE surfaces: a custom-built inert atmosphere chamber with a 400 nm optical cut-off filter (Newport FSQ-GG400) was placed on a conventional hotplate into a UV-curing chamber (Dymax 2000-EC). Commercially available permanent magnets (~ 0.5 T, K&J Magnetics BX088SH) were placed directly on the heating plate, followed by the PDMS negative mold, the LCE monomer mixture, and a coverslip (all held in place by Kapton[®]-tape). For more details, please refer to SI section 1.2.4. **b.** Diamagnetism and alignment of calamitic mesogen **1** ((4"-acryloyloxybutyl) 2,5-di(4'-butyloxybenzoyloxy)benzoate) in an applied magnetic field **B**. χ_{\parallel} and χ_{\perp} are the magnetic susceptibilities parallel and perpendicular to the LC mesogens principal axis, respectively. **n** denotes the LC director orientation. **c.** Schematic depiction of the arrangement of magnets and the LC-melt-filled PDMS mold to achieve an oblique alignment of the LC mesogens (corresponding to the case shown in Manuscript Figure 2 and Supplementary Figure 10) and z-alignment of LC mesogens (Supplementary Figure 8). PDMS and the coverslip are not shown in the schematic. To program molecular anisotropy oblique to the microstructure's principal axis, we first chose a director orientation of around the midpoint of 0° and 90° with respect to the Z-axis of the square micropost in the YZ-plane (indicated by the blue double arrow) as one would expect here the most pronounced tilting deformation upon the bulk order-to-disorder phase transition. (Note that magnetic field is only used during the fabrication and not in subsequent actuation process.) For quantitative calculation of the mesogen director orientation inside the microstructures, refer to the COMSOL Multiphysics methods that we previously reported⁶.



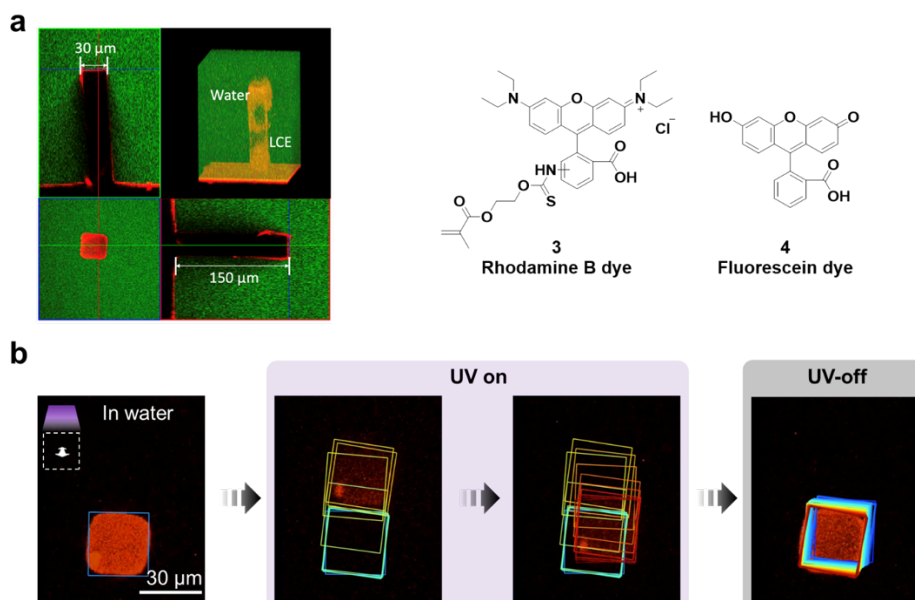
Supplementary Figure 4 | a. Phase behavior of the LC monomer mixture (prepared as described in SI section 1.2.3) measured by differential scanning calorimetry depicting the 2nd cooling cycle from 120 °C to -5 °C at 10 °C/min. The LC monomer mixture exhibits a nematic-to-isotropic phase transition temperature (T_{NI}) of 78 °C and a crystallization temperature (T_C) at 24 °C. **b.** Phase behavior of the UV-polymerized LCE (synthesized as described in SI section 1.2.4) measured by differential scanning calorimetry depicting the 2nd heating cycle from -5 °C to 200 °C at 10 °C/min. The LCE showed a glass transition temperature (T_g) of ~45 °C and a nematic-to-isotropic phase transition temperature (T_{NI}) of ~92 °C.



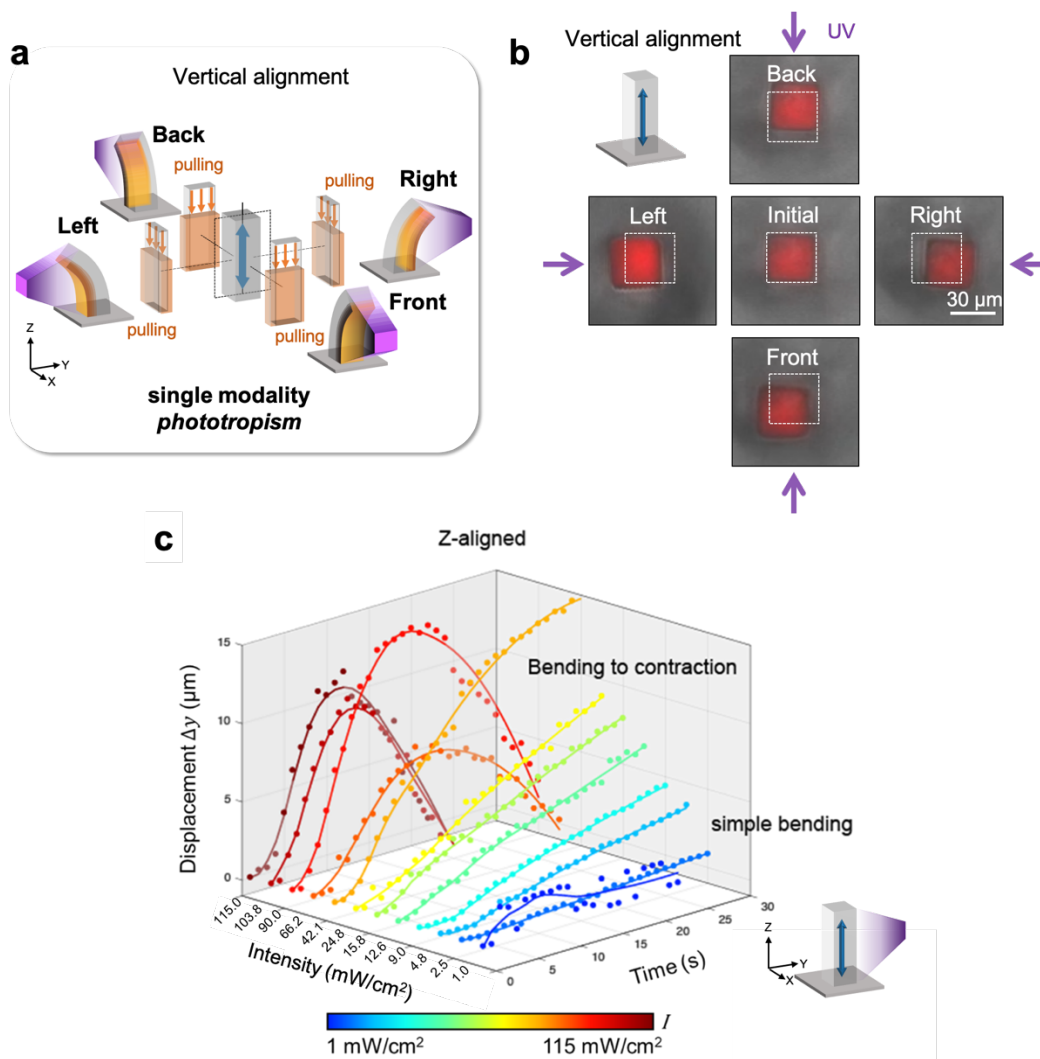
Supplementary Figure 5 | Representative absorption spectra for the photoisomerization of compound **2** (Synthon Chemicals, ST04181; λ_{max} = 361 nm, in dichloromethane; 293 K): **a.** Photoswitching from *trans*- to *cis*-isomer with 365 nm (ThorLabs, LED M365F1). **b.** Thermal relaxation from *cis*- to *trans*-isomer in the dark (PSS = photostationary state). **c.** Determination of the thermal half-life of the *cis*-isomer for compound **2** in dichloromethane (DCM) solution (as shown in part **b**) and in an LCE film at 60 °C: points correspond to measured data (observed at λ_{max} = 361 nm). The thermal half-life of the *cis*-isomer was determined to be $t_{1/2}$ ~9 s in dichloromethane solution and $t_{1/2}$ ~40 s in an LCE film at 60 °C. As one can tell from the comparison of the two, the thermal *cis*-to-*trans* relaxation rate strongly depends on the local molecular environment; dichloromethane as solvent was chosen for solubility.



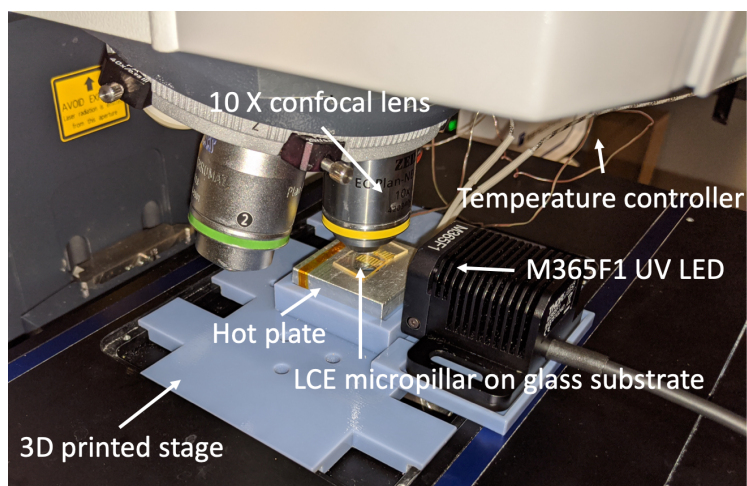
Supplementary Figure 6 | Thermal IR still images (FLIR A8303sc with 4x microscopy lens) of LCE microstructures with oblique-aligned LCE director on a heating stage set to 60 °C before and during in-plane UV-irradiation (115 mW/cm², M365F1 LED) from the left. No considerable photothermal heating is observed, which supports the notion that azobenzene crosslinker **2** mostly operates *via* photomechanical contraction^{13–15}. Because of the IR camera, the UV LED to sample distance was in this case more than usual.



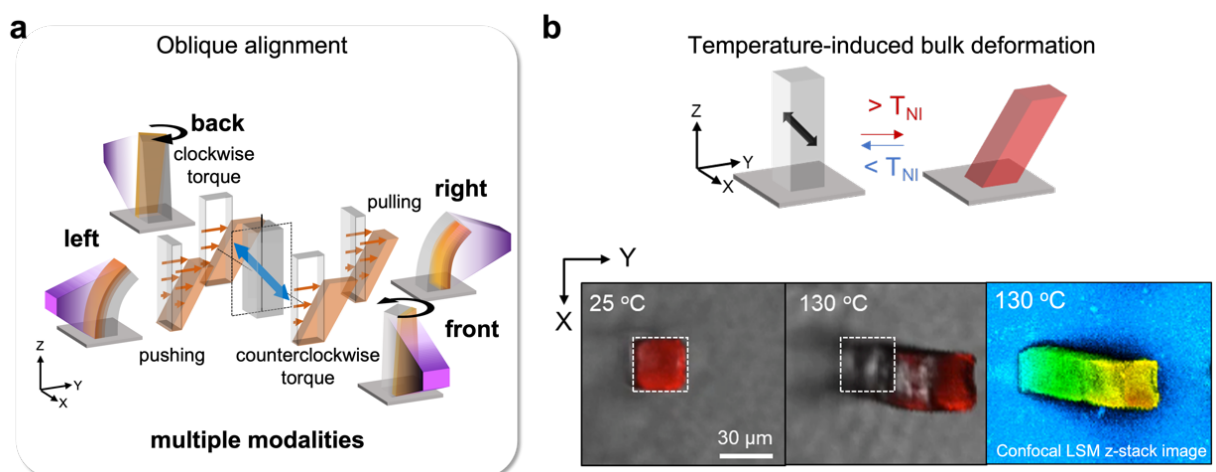
Supplementary Figure 7 | **a.** Z-stack of a square LCE micropost with oblique-aligned director orientation immersed in water. The image was obtained by confocal laser scanning microscopy (Zeiss, LSM700) with an immersion objective lens (Zeiss, W Plan-Apochromat 40x/1.0 DIC M27). The micropost was coated with Rhodamine B methacrylate **3** (shown in red, excited with $\lambda_{\text{ex}} = 555 \text{ nm}$) and the aqueous layer dyed with fluorescein **4** (shown in green, excited with $\lambda_{\text{ex}} = 488 \text{ nm}$). Note that water wets the microstructured surface well. **b.** Water acts as an effective heatsink and should thus suppress photothermal effects^{13–15}. UV-actuation (at 115 mW/cm², Thorlabs M365F1) depicted as still frames and image-tracked traces (petrol to red = UV on and red to blue = UV off) show a similar actuation path as in air (a non-monotonic light-seeking as expected for small θ). The sample was kept on a heating element set to 65 °C. The observed deformation was recorded with the fluorescein channel disabled. Despite water dissipating any local photothermal heating, significant deformation was seen which further confirms that the azobenzene crosslinker **2** does not operate *via* a photothermal actuation mechanism.



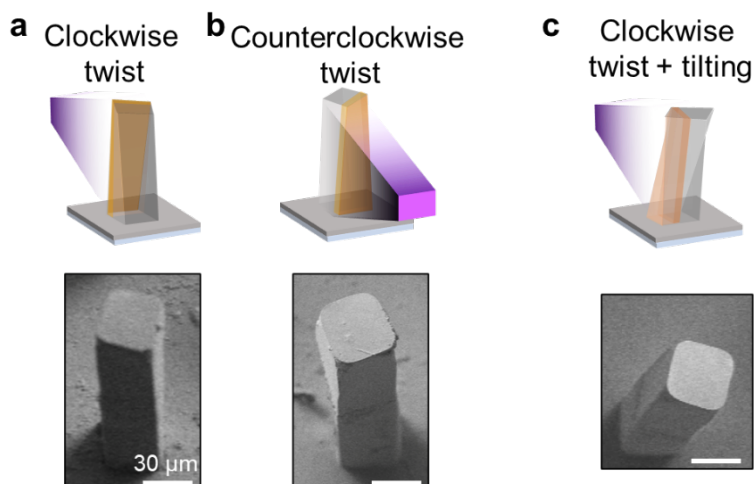
Supplementary Figure 8 | With an alignment along the principal symmetry axis, Z-alignment, only a single type of deformation—bending towards light—is expected, reminiscent of phototropism in nature¹⁶. **a.** Explanatory scheme to illustrate the origin of the observed phototropism: irrespective from what side the post is irradiated, in all cases the activated region at the irradiated face contracts along the Z-axis (illustrated with orange slabs), pulling on the ‘non-activated’ part (grey) and thus leading to bending towards light. **b.** Still frames from Supplementary Video 1 show ‘light-seeking’ deformation for UV-illumination from all four directions (back, right, front, and left; Thorlabs M365F1 at 15 mW/cm²). Posts were stained with methacryloxyethyl thiocarbamoyl rhodamine B (**3**, shown in red, excited with $\lambda_{\text{ex}} = 555 \text{ nm}$) for tracking *via* confocal fluorescence laser scanning microscopy. **c.** Quantification of photoactuation of a Z-aligned micropost under twelve different light-intensities ranging from 1 to 115 mW/cm² (1.0, 2.5, 4.8, 9.0, 12.6, 15.8, 24.8, 42.1, 66.2, 90.0, 103.8, and 115.0 mW/cm²). Under the low to medium intensity regime (1.0 to 42.1 mW/cm², blue to light orange in the diagram), the microposts exhibit a bending deformation towards the light source (light-seeking) with increasing amplitude as the UV intensity increases. As the intensity continues to increase (66.2 to 115.0 mW/cm²), a non-monotonic motion is observed, that constitutes initial light-seeking followed by reversal of bending direction to end up in a vertical, Z-contracted state, as governed by the director orientation. For more details on the image tracking, please refer to SI section 1.2.2.



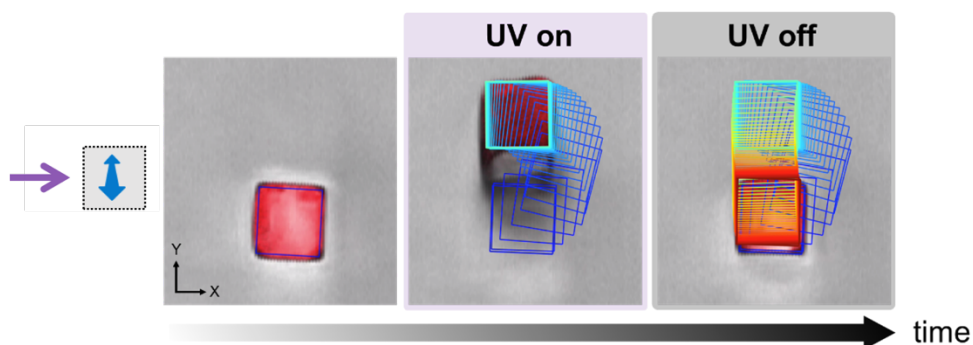
Supplementary Figure 9 | Custom-made imaging setup for confocal laser scanning microscopy comprising a 3D-printed sample stage, a temperature-controlled heating plate and slots to place the UV LED (Thorlabs M365F1). The LCE microstructures were heated to 60-70 °C (above their glassy state, $T_g \sim 45$ °C) for photoactuation with a UV LED.



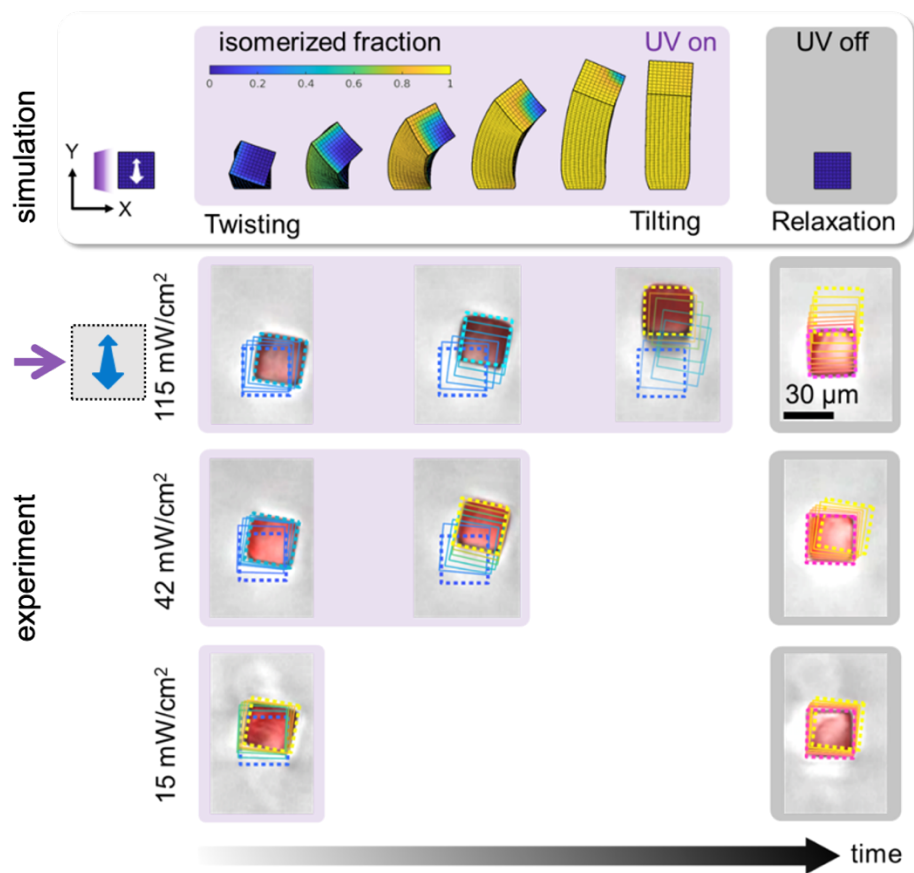
Supplementary Figure 10 | **a.** Upon breaking symmetry by tilting the director alignment away from the micropost principal symmetry axis to an oblique alignment, a multitude of deformations (light-seeking, light-avoiding, and twisting clock- and counterclockwise) are observed. The explanatory scheme illustrates the origin of the observed deformation behavior: all deformations are a result of the director-determined shearing to the right of the activated region (illustrated with orange slabs), which exerts different forces (pulling/pushing, orange arrows) and torques (clockwise/counterclockwise, orange arrows) on the ‘non-activated’ part (grey) of the micropost that depends on the facet of the structure being illuminated. Please also refer to Manuscript Figure 2 and Supplementary Video 1. **b.** Characteristic bulk shearing deformation of LCE microposts to the right with tilted (oblique) molecular alignment when heated above the nematic-to-isotropic transition temperature (T_{NI} , Supplementary Figure 4) at isotropic phase: A heating cycle (from 25 °C to 130 °C and back to 25 °C) confirms oblique bulk director alignment for the LCE square micropost, as above T_{NI} at isotropic phase, a clean thermal deformation (tilting) is observed. Posts were stained with methacryloxyethyl thiocarbamoyl rhodamine B (**3**, shown in red, excited with $\lambda_{ex} = 555$ nm) for tracking and 3D scanning (z-stack) *via* confocal fluorescence laser scanning microscopy (LSM).



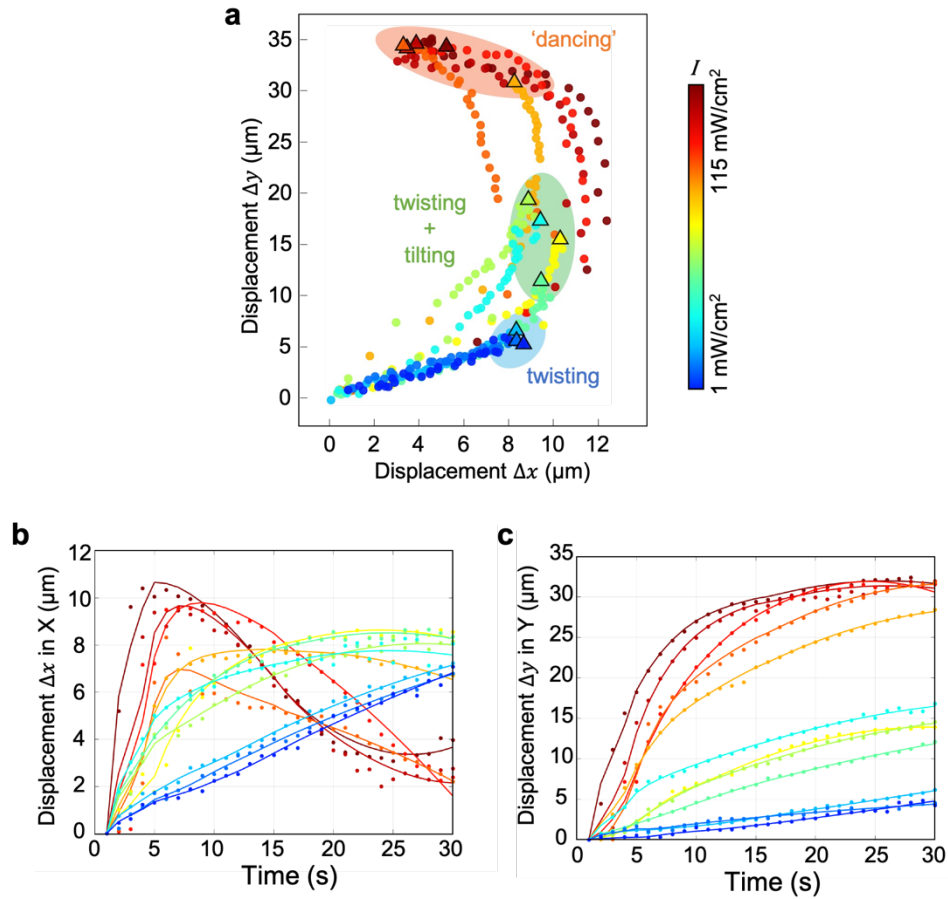
Supplementary Figure 11 | Kinetically trapped UV-deformed square microposts observed by field emission scanning electron microscopy (FESEM, Zeiss Supra 55 VP): **a-b.** low-intensity (15 mW/cm^2) UV illumination induced clockwise- and counterclockwise twisting (at 30° stage tilt), and **c.** medium-intensity (42 mW/cm^2) UV illumination triggered combination of clockwise twisting and tilting (at 15° stage tilt). The deformed LCE microposts were ‘frozen’ to fix the actuated shape in the glassy state of the LC elastomer by rapidly cooling from 60°C to room temperature, which is below its glass transition temperature (T_g) of $\sim 45^\circ \text{C}$ (Supplementary Figure 4). The trapped LCE microposts were coated with 10 nm Pt/Pd (80:20) by sputter coating prior to imaging.



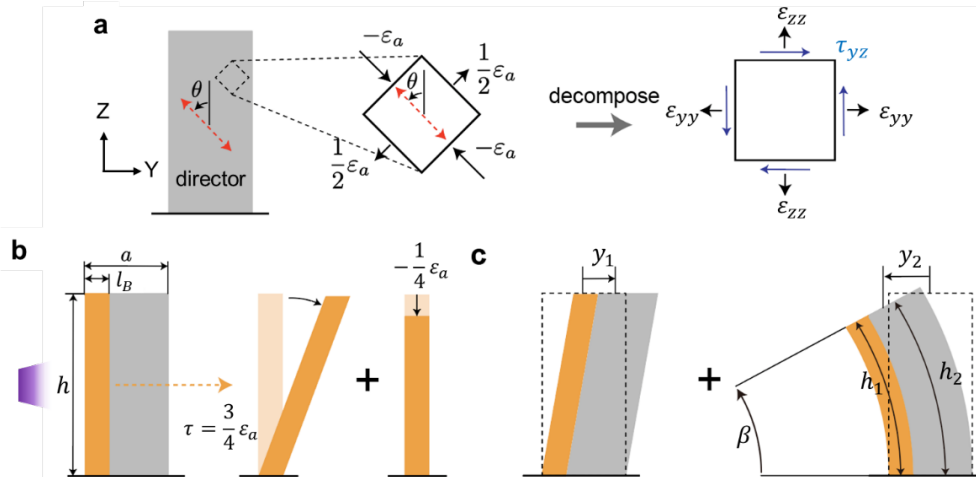
Supplementary Figure 12 | Example of image-tracking procedure: Fluorescent images used for image tracking (using a MATLAB script) and resulting fitted squares depicted as trace of a ‘dancing’ micropost (from blue to turquoise to orange). Each colored square corresponds to one fluorescent image. Note that in Manuscript Figure 3a and Supplementary Figure 13 not all tracked squares are displayed for better visualization. For more details, please refer to SI section 1.2.2.



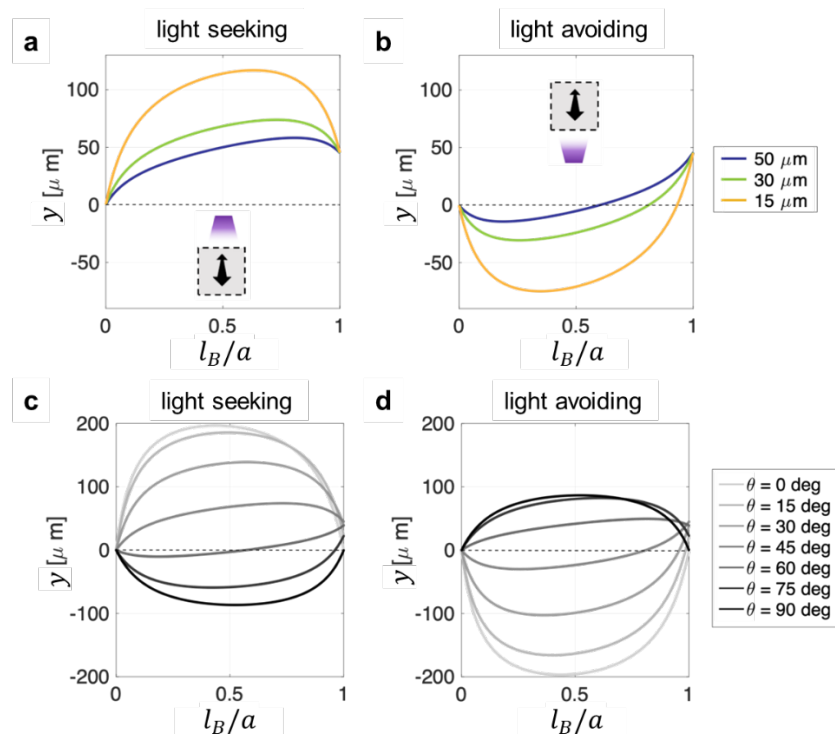
Supplementary Figure 13 | Comparison of simulated and experimental results demonstrating the characteristic non-linear motion trajectories of a micropost with oblique alignment and out-of-plane irradiation. UV-actuation at low (15 mW/cm²), medium (42 mW/cm²), and high (115 mW/cm²) light intensity triggers non-linear deformation trajectories ranging from simple twisting to twisting and bending to ‘dancing’. The still-frames are taken from Supplementary Video 2 with illumination along the X-axis. Stills of the finite element simulation are shown for comparison (Manuscript Figure 3a & b and SI Section 2.1 for more details). Posts were stained with methacryloxyethyl thiocarbamoyl rhodamine B (**3**, shown in red, excited with $\lambda_{\text{ex}} = 555 \text{ nm}$) for tracking *via* confocal fluorescence laser scanning microscopy.



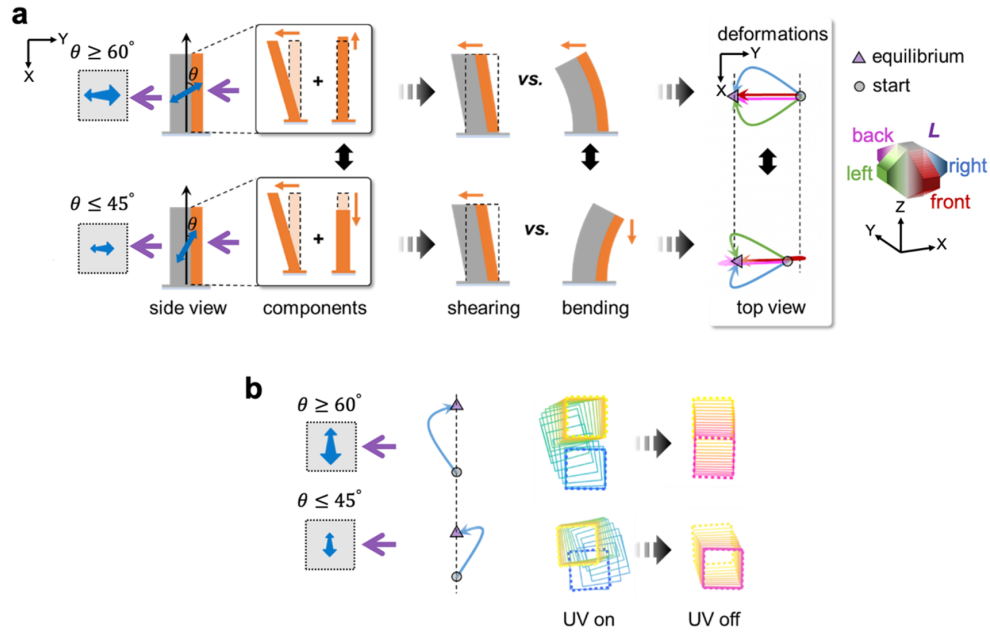
Supplementary Figure 14 | Quantification of the non-linear deformation trajectory of the micropost an oblique-aligned director (Manuscript Figure 3d) with regard to the tip displacement along the X- and Y-axis for twelve different light-intensities ranging from 1 to 115 mW/cm² (1.0, 2.5, 4.8, 9.0, 12.6, 15.8, 24.8, 42.1, 66.2, 90.0, 103.8, and 115.0 mW/cm²). **a.** Comparison of the elicited trajectories in the XY-plane; **b.** Corresponding time-traces for the displacement along the X-axis. **c.** Corresponding time-traces for the displacement along the Y-axis. As light intensity is increased, the maximum amplitude of post deformation (both in X and Y direction) is reached more quickly. For more details on the image tracking, please refer to SI section 1.2.2.



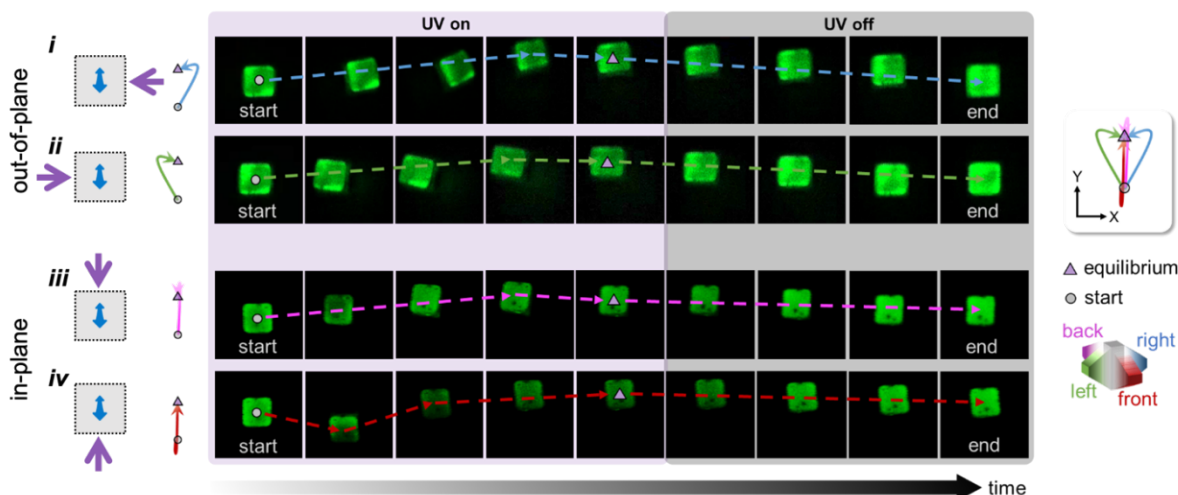
Supplementary Figure 15 | Theoretical model to explain the non-linear behavior for light-seeking and light-avoiding in microposts with oblique director alignment. **a.** Transformation of strain state from director frame to YZ frame to facilitate analysis. **b.** The deformation of the UV-actuated layer (depicted in orange) can be divided into two parts: shearing and contraction. **c.** The deformation of the 'activated' layer results in two different deformation modes of the entire post: shearing and bending. For more details, please refer to SI Model 2, section 2.2.



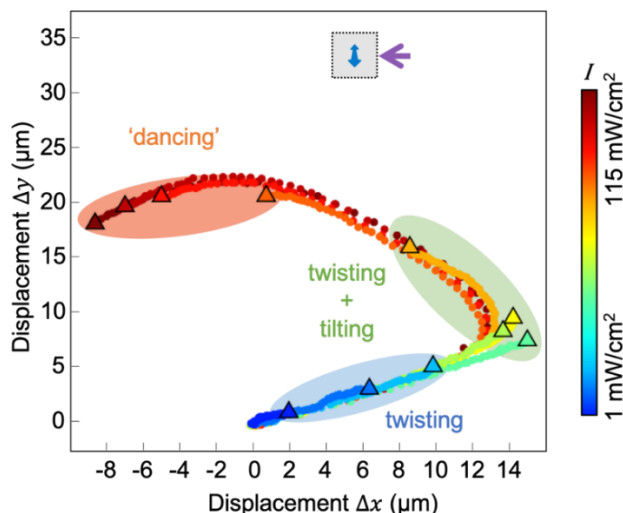
Supplementary Figure 16 | Theoretical model to account for the non-linear actuation behavior of microposts with oblique director alignment in the 'light-seeking' and 'light-avoiding' case (please refer to SI Model 2, section 2.2 and Supplementary Figures 17-19). **a-b.** Influence of post size (from 15 to 50 μm side length) on the tip motion of the micropost for 'light-seeking' (**a**) and 'light-avoiding' (**b**) behavior. **c-d.** Influence of director orientation (defined as director tilted at an angle θ away from Z-axis in the XZ-plane) on the tip motion of the post for **c**, 'light-seeking' (**c**) and 'light-avoiding' (**d**) behavior.



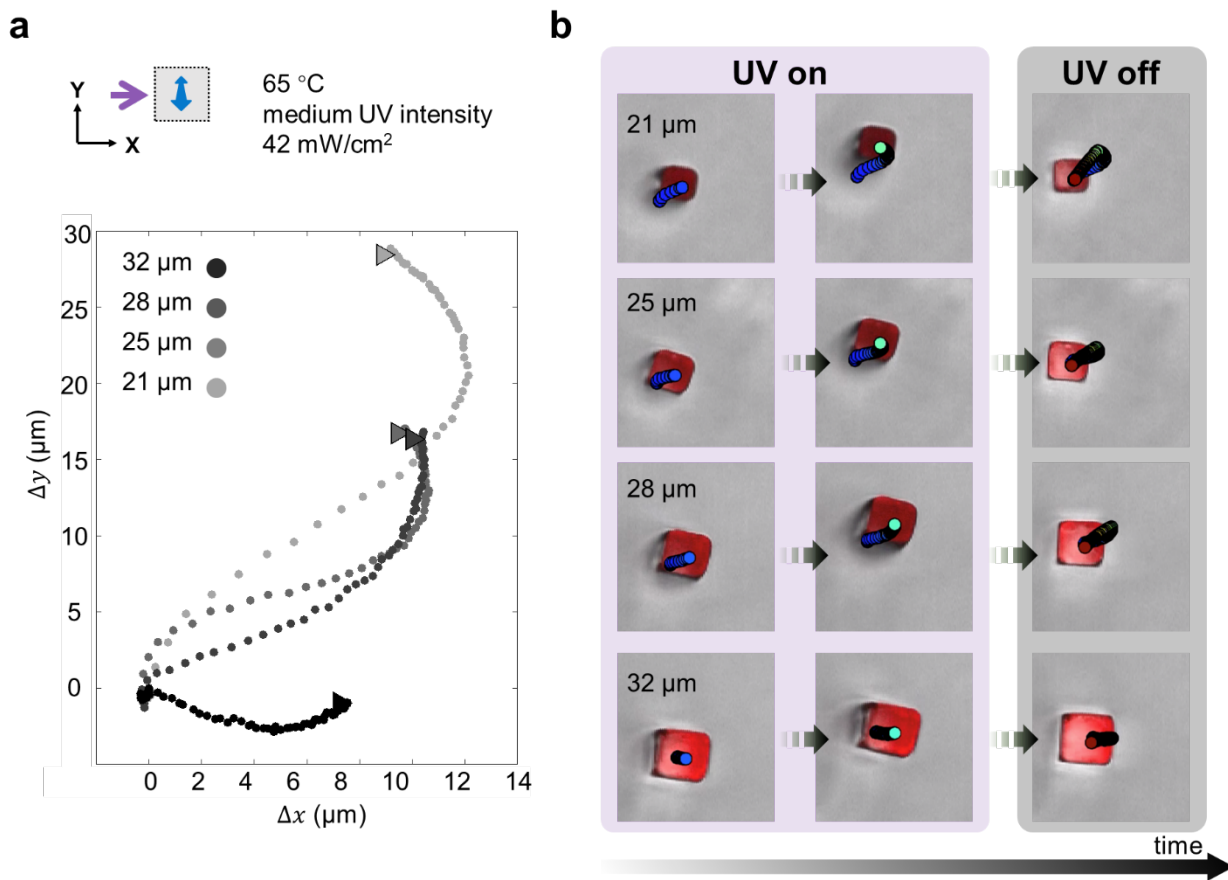
Supplementary Figure 17 | Effect of tilt of director orientation on deformation behavior of LCE microposts with oblique molecular alignment. While the final positions of the deformed posts under high-intensity UV-irradiation (115 mW/cm^2) are similar (identical to the deformed posts after thermal nematic-to-isotropic phase-transition, see e.g. Supplementary Figure 10b), the deformation trajectories to that final sheared deformation state vary starkly depending on the tilt of the director alignment and the direction of illumination (Manuscript Figure 3e): **a**. Deformations of the ‘activated’ layer for the oblique-aligned director contain two components, a shearing component (along the Y-axis) and a contracting/expanding component (along the Z-axis). A contraction along the Z-axis is expected for a director of $\theta \leq 45^\circ$, whereas an expansion is expected for a director $\theta \geq 60^\circ$. These opposite behaviors will lead to ‘dancing’ toward or away from the light source, respectively. Note the switch of the ‘green’ (irradiation from left) and ‘blue’ (irradiation from right) deformation trajectories for the two cases. The circle corresponds to the post starting position; the triangle denotes maximum displacement under irradiation. **b**. A change in director tilt causes a change from ‘dancing away’ to ‘dancing towards’ light for out-of-plane irradiation as the director alignment crosses a threshold between $\theta = 45^\circ$ – 60° . Tracked experimental deformation trajectories are depicted to illustrate these two types of behaviors.



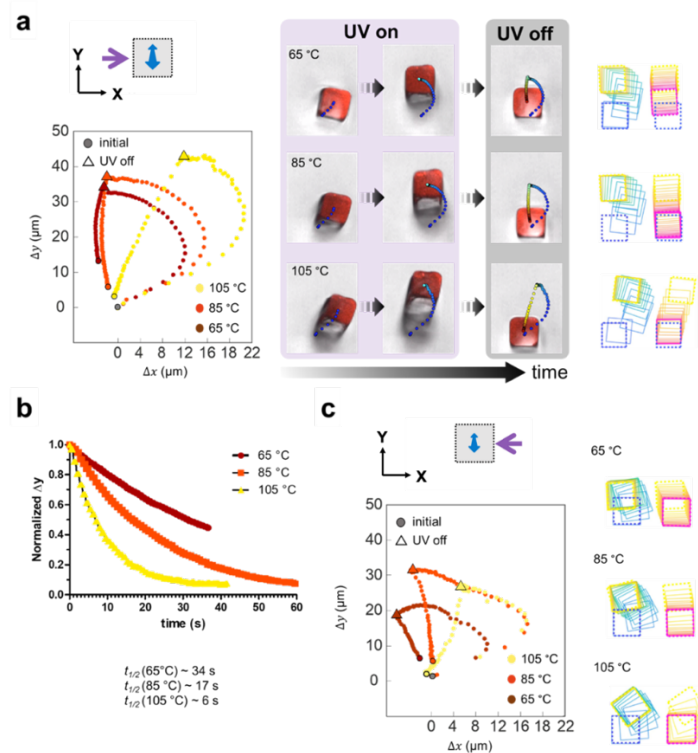
Supplementary Figure 18 | Confocal fluorescence laser scanning microscopy top-view still images depicting post deformations for UV-illumination from four directions (*i*) right, (*ii*) left, (*iii*) top, and (*iv*) bottom for the case of a molecular anisotropy tilted at $\theta \leq 45^\circ$ (steep director orientation). Note that in the case of in-plane irradiation (*iii* & *iv*) the horizontal (pushing or pulling) and vertical (expanding) components may act either in a supportive (light-seeking case, *iii*) or in a counteractive fashion (light-avoiding case, *iv*) leading to pronounced reversal of deformation direction along the Y-axis. Posts were stained with methacryloxyethyl thiocarbamoyl rhodamine B (**3**, shown in green, excited with $\lambda_{\text{ex}} = 555 \text{ nm}$) for tracking *via* confocal fluorescence laser scanning microscopy. For annotation, the circle corresponds to the post starting position; the triangle denotes maximum displacement under irradiation.



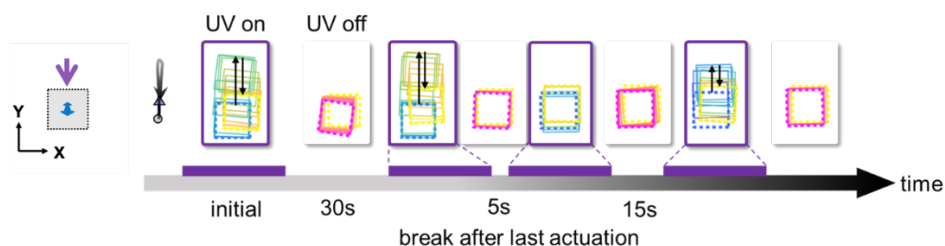
Supplementary Figure 19 | Quantification of the non-linear deformation trajectory of a micropost with a steeper oblique-aligned nematic director, tracing its displacement along the X- and Y-axes for eleven different light intensities ranging from 1 to 115 mW/cm^2 (1.0, 2.5, 4.8, 12.6, 15.8, 24.8, 42.1, 66.2, 90.0, 103.8, and 115.0 mW/cm^2). Note that the molecular director orientation is slightly tilted out from the YZ-plane, which causes a displacement along the X-direction in the fully illuminated state. The extent of the final X-displacement can be programmed by controlling the director orientation in the XZ plane. For more details on the image tracking, please refer to SI section 1.2.2.



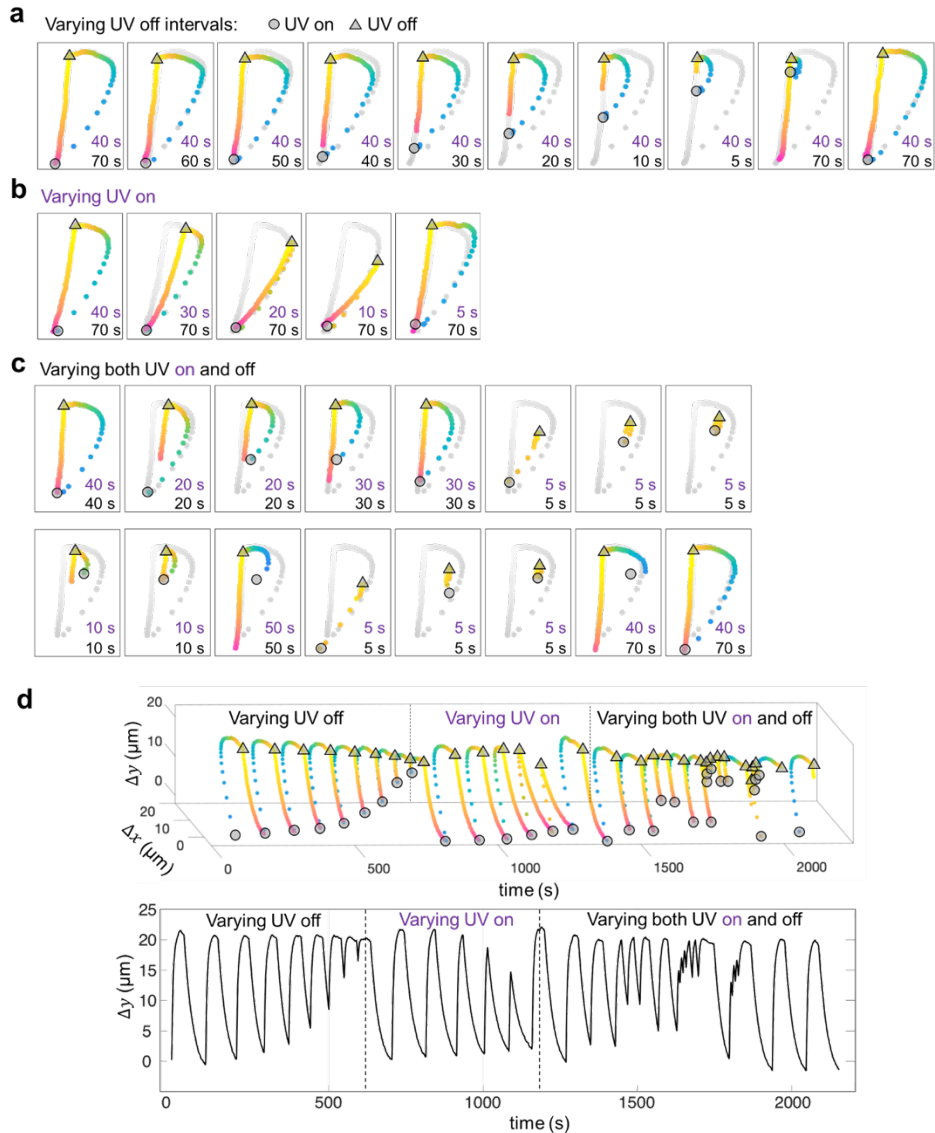
Supplementary Figure 20 | Quantification of the size-dependent deformation trajectories for microposts with oblique-aligned director ($\theta \geq 60^\circ$) at medium light intensity (42 mW/cm²). The deformation trajectory of LCE microposts of varying sizes (21, 25, 28, and 32 μm , respectively) changes drastically as a result of changes in bending stiffness and propagation dynamics of the traveling isomerization wave (Manuscript Figure 3f). **a**. Deformation trajectories of the micropost tip obtained through image tracking. **b**. Confocal fluorescence laser scanning microscopy top-view still images for the four post thicknesses and overlaid imaged tracking for the center of the top face of the post. Pillars were stained with methacryloxyethyl thiocarbamoyl rhodamine B (**3**, shown in red, excited with $\lambda_{\text{ex}} = 555 \text{ nm}$). See also Supplementary Video 4.



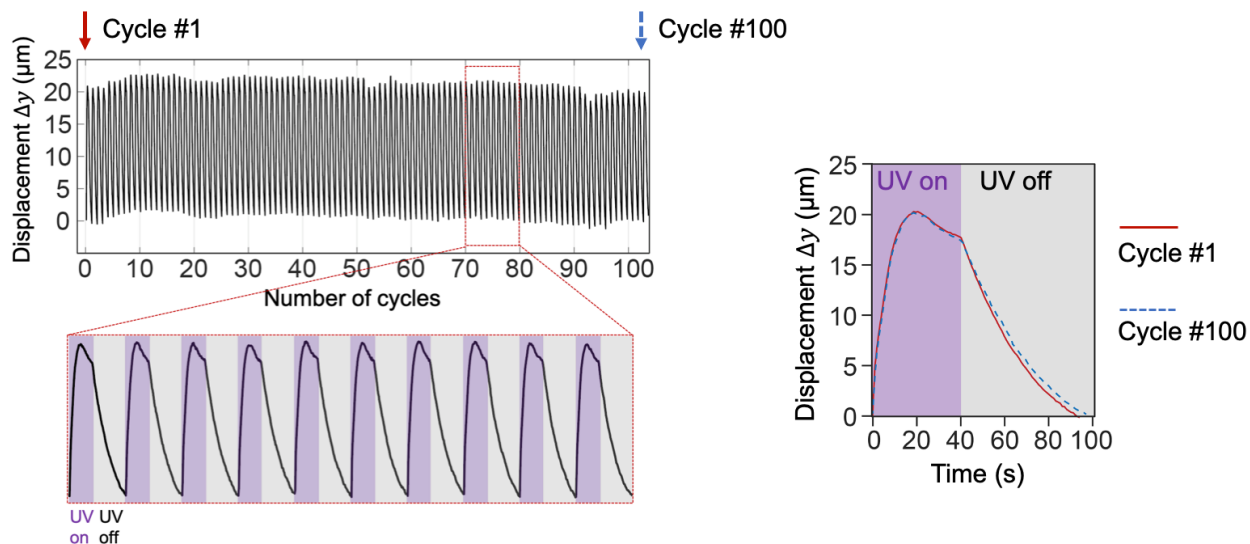
Supplementary Figure 21 | Quantification of the temperature dependence of deformation trajectories for microposts with an oblique-aligned director (Manuscript Figure 3g). Under high-intensity (115 mW/cm^2) irradiation, increasing the temperature of the sample stage (from 65°C to 105°C) decreases material stiffness and speeds up the *cis*-to-*trans* thermal relaxation of the azobenzene crosslinker, reducing the photostationary state reached and restricting progression of the traveling isomerization front. As a result, deformations of obliquely aligned samples at 105°C show larger initial amplitudes. **a**. Temperature-dependent behavior for flatter director tilt ($\theta \geq 60^\circ$). **b**. Fitting of the normalized Y-displacement for the thermal recovery data presented in **a** with a single exponential process upon switching off the UV-irradiation ($t_{1/2} \sim 34$ s at 65°C , ~ 17 s at 85°C , and ~ 6 s at 105°C). **c**. Temperature-dependent behavior for a steeper alignment (closer to Z-alignment, $\theta \leq 45^\circ$). See also Supplementary Video 4.



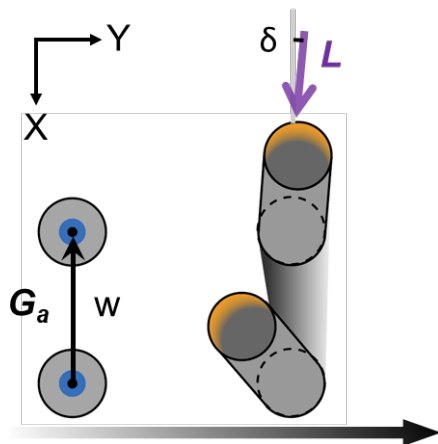
Supplementary Figure 22 | Refractory period observed in photoactuations: Image tracking of the deformations shown in Supplementary Video 5 for in-plane UV-irradiation of an oblique-aligned micropillar ($\theta \leq 45^\circ$) submerged in water (to exclude any possible heating effects). Due to the non-instantaneous *cis*-to-*trans* thermal recovery of the photoswitchable crosslinkers, the ability of a pillar to undergo photoactuation directly after an excitation period is diminished as demonstrated with varying lengths of UV 'off' intervals in between UV 'on' periods. Also refer to Manuscript Figure 3h for quantification of deformation amplitudes. The microposts were immersed in water throughout the measurement. A comparable behavior is observed also in air.



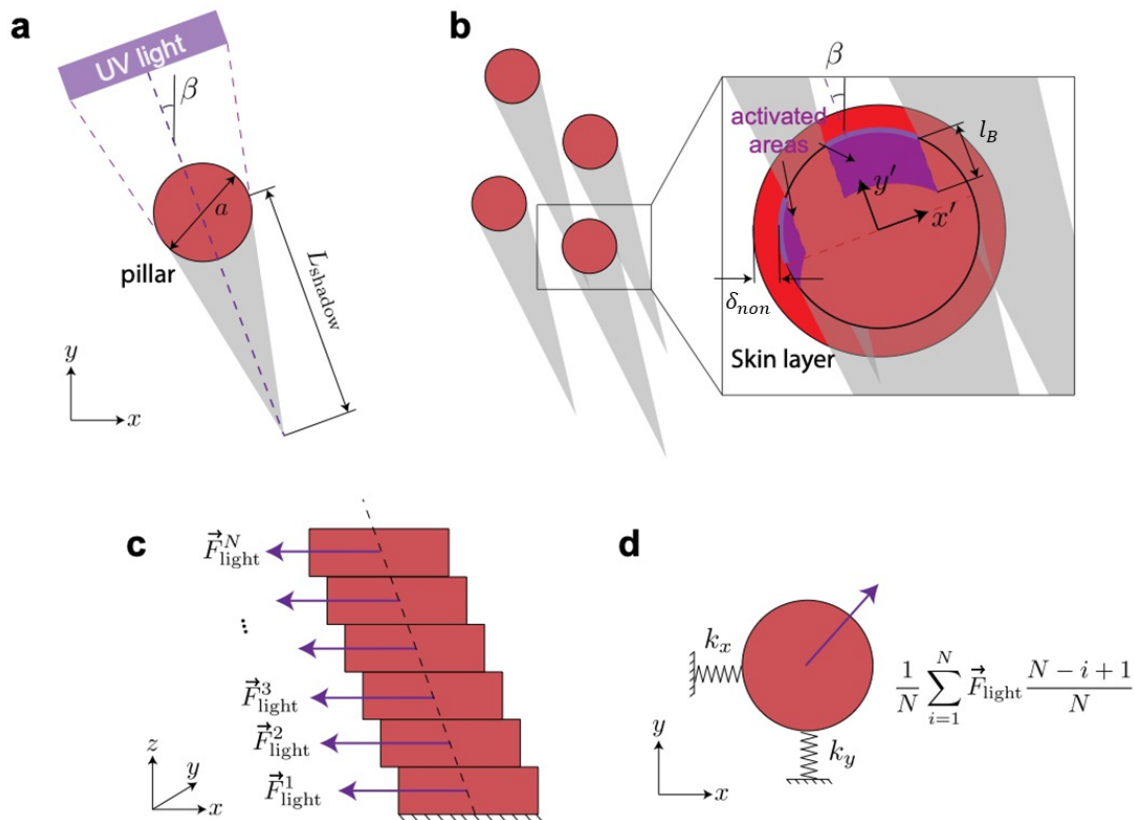
Supplementary Figure 23 | Deformation trajectories for a single oblique-aligned micropillar modulated by changing the (out-of-plane) irradiation on-off intervals at high light intensity (115 mW/cm^2), harnessing the effects of non-instantaneous thermal relaxation of the *cis*-azobenzene population as illustrated in Supplementary Figure 22. **a**. For cycles of out-of-plane irradiation, when the UV irradiation times are kept constant, but relaxation times are gradually shortened, the final position of the pillar remains the same, but the starting position of each cycle moves towards the tilted state. Full amplitude actuation was resumed after complete relaxation (UV off 70 s). **b**. In contrast, when the relaxation time is kept constant, but UV irradiation times are consecutively shortened, the starting position remains the same, but the end position moves along the trajectory at full amplitude. Triangles denote maximum post displacement before switching the UV-irradiation off. **c**. Both the starting and end positions can be tuned by varying the irradiation on and off intervals. **d**. 3D traces of the photoactuation paths along both X- and Y-directions as a function of time for actuation pathways in **a-c**, top row, and 2D traces of the Y-displacement as a function of time, bottom row, illustrate the dynamic and highly programmable deformation behaviors (Supplementary Video 5).



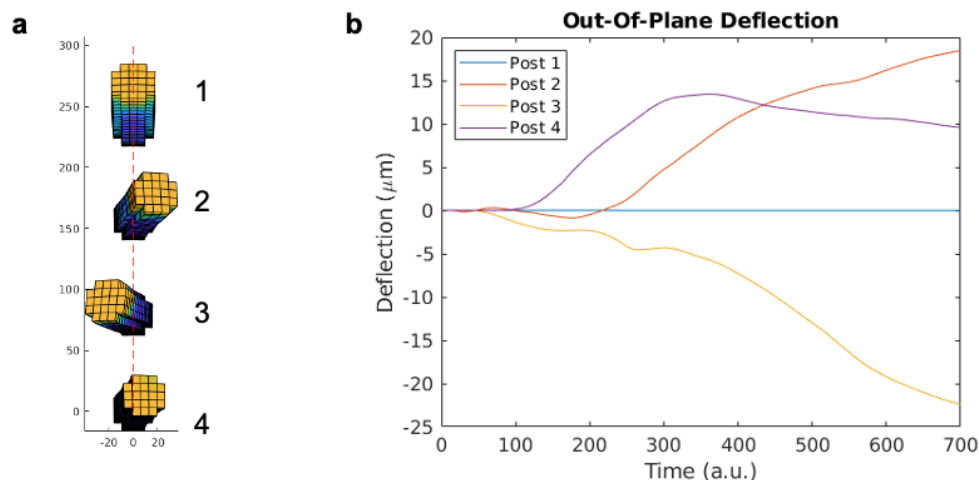
Supplementary Figure 24 | No appreciable fatigue is observed over at least 100 consecutive cycles of photoactuation at 115 mW/cm^2 for the example of out-of-plane ‘dancing’ behavior with UV ‘on’ 40 s and UV ‘off’ 60 s in each cycle at $60 \text{ }^\circ\text{C}$. These results indicate that photodegradation effect is insignificant under the conditions studied.



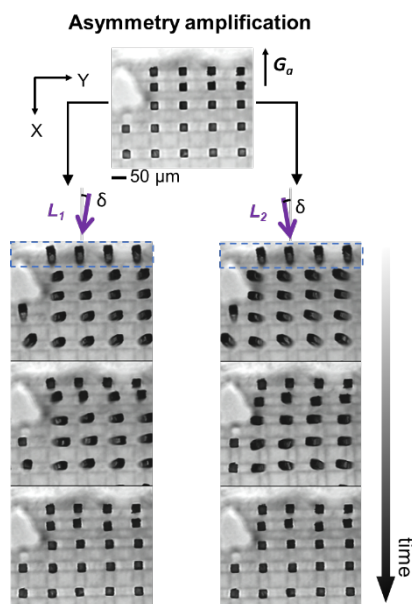
Supplementary Figure 25 | Schematic illustration of the origin of pattern formation in arrays of Z-aligned microposts (Manuscript Figure 4a): Under experimental conditions that favor stable bimorphs, even a small misalignment between \mathbf{G}_{array} and \mathbf{L} causes symmetry breaking that can lead to starkly different deformations of posts along the array. As the first post bends towards the light along \mathbf{L} with a small angle δ to the array axis \mathbf{G}_{array} , the subsequent post gets exposed to light only partially, promoting its out-of-plane bending, which gets amplified, the more the post deforms. The resulting location-dependent symmetry-breaking and deformation creates stable, self-organized patterns along the post array. Note that the velocity of propagation of the order-to-disorder front within each pillar can be different from the velocity of deformation along the array.



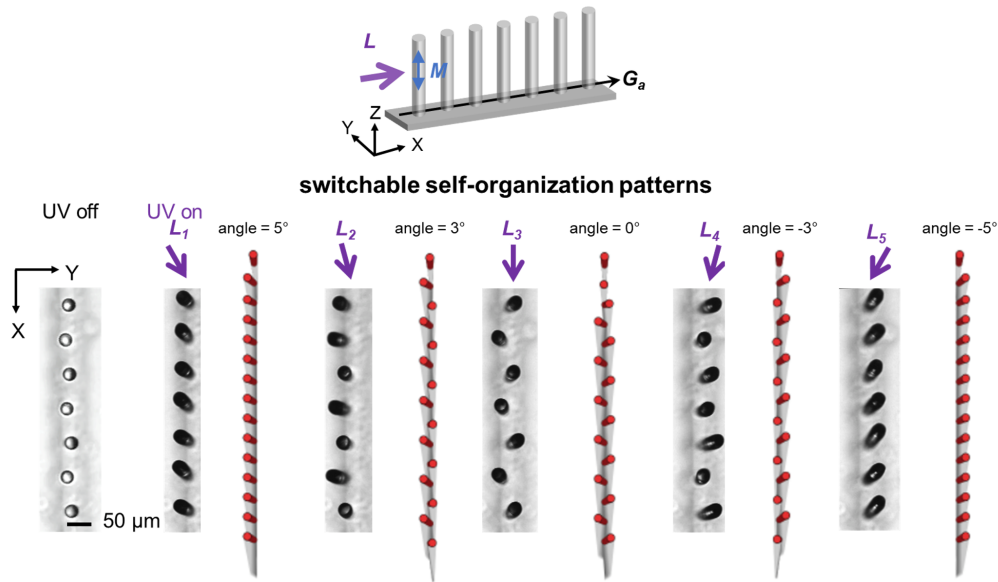
Supplementary Figure 26 | Discrete model to capture the collective deformation response of micropost arrays under UV light from different angles. **a.** The cylindrical post shades a triangular shadow against the UV light. **b.** For each post, the shadow from other posts blocks UV light. As a result, only part of the post is activated, considering penetration depth l_B and a ring of non-excitabile material given by δ_{non} . **c.** We discretize the post as a stack of disks and each layer exerts an equivalent light-induced activation force. **d.** The total force is balanced by two linear springs to yield the final top displacements of the posts. For more details, please refer to SI Model 3, section 2.3.



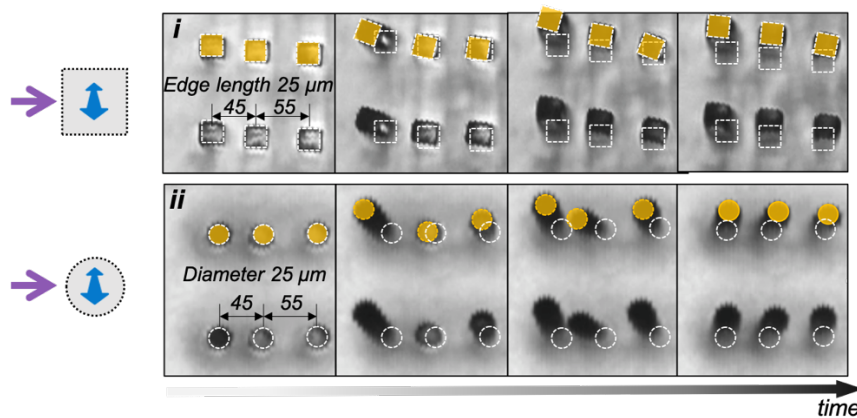
Supplementary Figure 27 | Simulated deformation of circular microposts within an array (Supplementary Video 6). Posts are subject to irradiation from two light sources offset by $\pm 1^\circ$ offset to the array axis. Post dimensions correspond to a height of $150\ \mu\text{m}$ and diameter of $30\ \mu\text{m}$, with a center-to-center separation of $78\ \mu\text{m}$ along the array. **a**. The nematic director is oriented along the vertical (Z-)axis of the posts, resulting in phototropic bending. Light vectors are propagated through the finite elements as described in Model 1. **b**. Out-of-plane (out-of-string) deformation through time for the four posts.



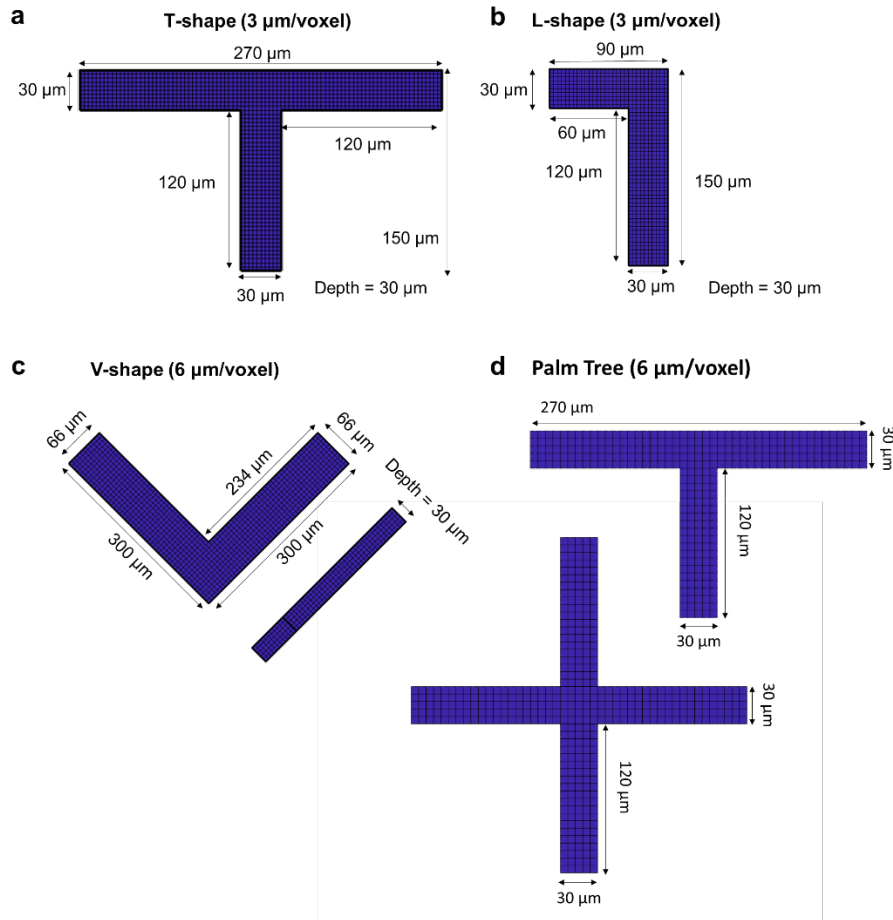
Supplementary Figure 28 | A clear asymmetry amplification effect is observed in an array of square microposts with mesogenic alignment along the Z-direction: for the same array, when light is along the X-axis with just a small negative/positive angle δ with regard to the X-axis (corresponding to G_a), amplification of the asymmetry is observed as the amplitude of out-of-plane deformation increases along the array. As δ is very small, no noticeable difference in light-seeking deformation is observed for first row of posts (marked with a blue dashed box). However, subjacent rows of posts are exposed to light asymmetrically because of interpost communication, amplifying the deformation out of plane. Temperature $60\ ^\circ\text{C}$.



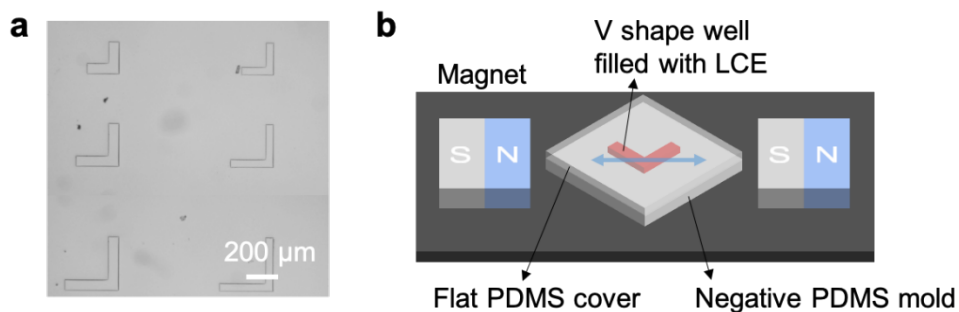
Supplementary Figure 29 | Variation of the angle of irradiation L with respect to G_a , creates different self-organized patterns of deformations under experimental conditions that favor stable bimorphs. While L_1 and L_5 show near-uniform out-of-plane bending (compare to the amplification observed in Supplementary Figure 28), undulating wave-patterns of different accentuation are formed for angles associated with L_2 , L_3 , and L_4 . The angles of purple arrows are exaggerated for illustration purposes. Formation of such wave-like patterns is highly reproducible. See also Supplementary Video 6.



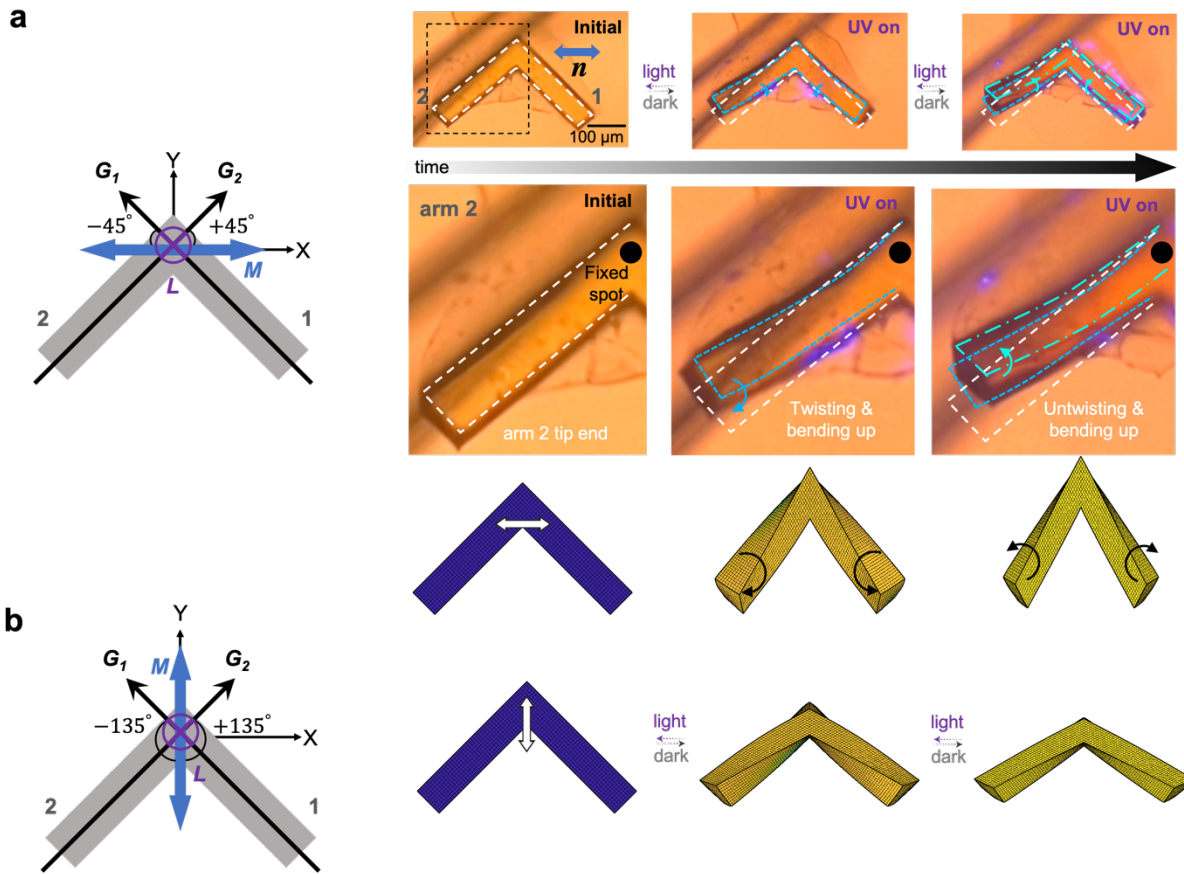
Supplementary Figure 30 | Spacing-dependent interpost communication in arrays of microposts of square and circular shape with an oblique director orientation, under conditions that allow for dynamic bimorph propagation ($60\text{ }^\circ\text{C}$). In strings of posts with an array axis G_a orthogonal to the oblique director alignment M with variable interpost spacings (increasing from $45\text{ }\mu\text{m}$ to $55\text{ }\mu\text{m}$ and larger), strong coupling between posts located in close proximity is observed. Experimental still images demonstrate that when irradiated along the row of microposts, the post closest to the light source undergoes the characteristic non-linear ‘power stroke’ trajectory, while the post shadowed by the first starts moving with a time-delay, once the first post bends out of the way. Due to the presence of the first post only part of the second post is exposed to light and hence its ‘power stroke’ differs from the first.



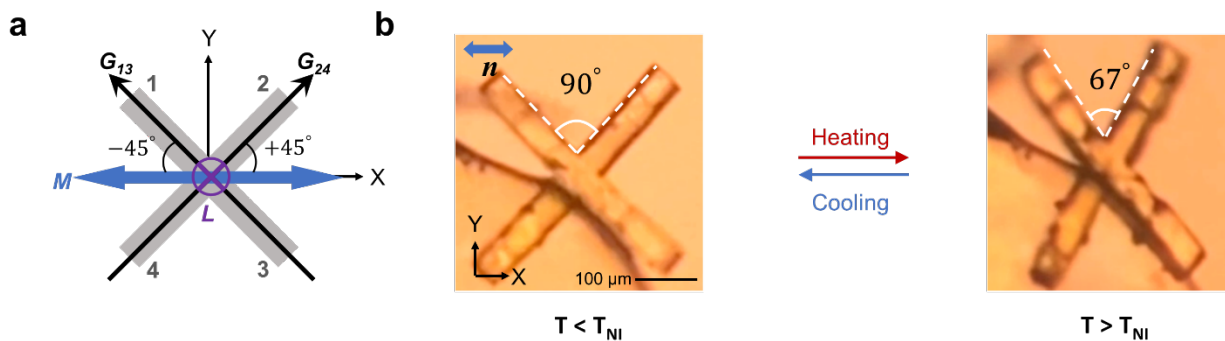
Supplementary Figure 31 | Dimensions of the simulated **a.** T-shaped, **b.** L-shaped, **c.** V-shaped, and **d.** Palm-tree-shaped structures discussed in Manuscript Figure 5b. Code units were chosen to correspond to a resolution of one finite element voxel per 3 μm in **a** & **b** and per 6 μm in **c** & **d**.



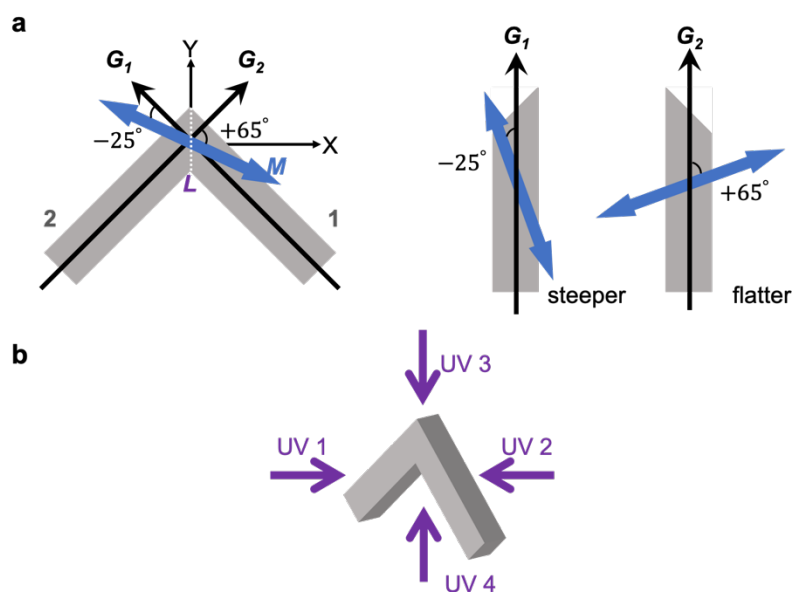
Supplementary Figure 32 | **a.** Optical micrograph of the PDMS mold with 'V' shape patterns of different dimensions: 75 x 200, 50 x 200, 75 x 300, 50 x 300, 75 x 400, and 50 x 400 μm (from top-left to bottom-right). All 'V' shaped jointed microstructures are 70 μm in depth (calculated from the SEM tilted-view image of the corresponding silicon master). **b.** Schematic depiction of the experimental setup for the magnetic alignment of freestanding 'V' shape LCE actuator. The polymerization was conducted following the same procedure as shown in Supplementary Figure 3 and SI section 1.2.3-1.2.5.



Supplementary Figure 33 | Freestanding single-material jointed V-shaped microstructures exhibit programmable twisting, bending, and shearing deformations. **a.** Design of a V-shaped LCE actuator containing two structural axes $\mathbf{G}_{segment-1}$ and $\mathbf{G}_{segment-2}$ (oriented along the two diagonals of the coordinate system). The structure has a uniform molecular alignment \mathbf{M} along the X-axis, however the relative angles between \mathbf{M} and the respective geometrical axes $\mathbf{G}_{segment}$ have opposite signs ($+45^\circ$ vs. -45°), which leads to opposite twisting and an overall closing motion (relative inwards shearing) of the two arms (segments) when illuminated along the Z-axis. As the light penetrates deeper into the thickness of the V-structure, the two arms begin to untwist, similar to what is observed in single microposts (Manuscript Figure 3a). Top row shows experimental optical microscopic images. Zoomed-in images of arm 2 in the middle row show a clear twisting and untwisting along with upwards bending of the arm tip. Bottom row shows stills from the finite element (FE) simulation. Please also refer to Supplementary Video 9&10. The black circle at the V-shape joint indicates the anchoring spot of the V-actuator to a capillary tube for hanging the structure in air. **b.** A V-shaped actuator with molecular alignment along the Y-axis (instead of X-axis) undergoes outwards twisting and opening of its two arms when illuminated along the Z-axis, as predicted by the FE simulation.



Supplementary Figure 34 | Freestanding jointed X-shaped microstructure with molecular alignment M along the X-axis (a) undergoes only shrinkage along the director upon heating (from 25 °C to 130 °C and back to 25 °C), changing the X-shape to a 'slender' X-shape (b). Compare to the range of twisting, bending and shearing motions that the segments of the V-shape and X-shape display upon UV radiation (see Supplementary Figure 33 and Figure 5a in the Main text).



Supplementary Figure 35 | When the molecular alignment is offset with regard to the X-axis in a jointed microstructure of V-shape, the uniform bulk director orientation M forms different angles with $G_{segment}$, G_1 and G_2 . As a result, these two segments (arms) exhibit different stroke-like deformations either toward ($\theta \leq 45^\circ$) or away from the light ($\theta \geq 60^\circ$) for out-of-plane irradiation (UV 1 and UV 2). Similarly, the arms will behave differently for in-plane irradiation (UV 3 & UV 4). Please also refer to Manuscript Figure 3e for a detailed discussion on the influence of director tilt and different illumination directions in a square micropost on the post's deformation behavior.

4 Supplementary Videos

Supplementary Video 1 | Single deformation mode vs multi-modal deformations under mild UV intensity (15 mW/cm²). **Left:** Top view of light-responsive deformation of Z-aligned LCE square micropost exhibiting only one deformation mode – bending towards the light – for all illumination directions (see also Supplementary Figure 8). **Right:** Top view of light-responsive deformation of LCE square micropost with oblique mesogen alignment exhibiting different deformation modes: clockwise twisting (irradiation from back), ‘light-seeking’ (irradiation from right), counterclockwise twisting (irradiation from front), and ‘light-avoiding’ (irradiation from left). Please also refer to Figure 2 in the main text and Supplementary Figures 10-11).

Supplementary Video 2 | Light intensity-dependent self-regulated non-linear actuation. Qualitative agreement of experimentally observed and theoretically predicted (Finite Element simulations, SI section 2.1) micropost deformations for LCE microposts with oblique mesogen alignment irradiated out-of-plane at high- (115 mW/cm²), medium- (42 mW/cm²), and low- (15 mW/cm²) light intensity. Simulation results were rescaled in time to match the experiment. Color scale corresponding to collective *trans*- (blue) to *cis*- (yellow) photoisomerization of the azobenzene cross-linker.

Supplementary Video 3 | Photoactuation of an LCE square micropost with oblique mesogen alignment illuminated from opposite directions at high light-intensity (115 mW/cm²) results in mirrored stroke-like deformation trajectories.

Supplementary Video 4 | Effect of geometry and temperature on the light-responsive deformation of microposts with oblique mesogen alignment. **Top:** Top view of deformation trajectories for LCE microposts of different edge lengths (32, 28, 25, and 21 μm, from left to right) under medium light intensity (42 mW/cm²) (Supplementary Figure 20, Manuscript Figure 3f). **Bottom:** Top view of deformation trajectories for LCE microposts actuated at different temperatures under high (115 mW/cm²) irradiation intensities (Supplementary Figure 21, Manuscript Figure 3g).

Supplementary Video 5 | Effect of irradiation duration and intervals. **Left:** Top view of light-responsive ‘light-seeking’ deformation of LCE square microposts with steeper oblique mesogen alignment immersed in water (Supplementary Figure 22) under in-plane irradiation at high light intensity (115 mW/cm²) with varying time breaks in between actuation cycles (30s, 5s, then 15s). A reduction in deformation amplitude was observed with shorter time breaks in between two illumination periods (Manuscript Figure 3h). **Right:** Top view of out-of-plane ‘dancing’ deformations of a photoresponsive oblique-aligned micropost modulated by changing the irradiation ‘on’-‘off’ intervals at high light intensity (115 mW/cm²). Depending on the duration of the interval of irradiation or relaxation, various starting and end positions can be sampled. Please refer to Supplementary Figure 23 for more details on lengths of UV-‘on’ and UV-‘off’ in each cycle.

Supplementary Video 6 | Self-sorted patterns appearing in microstructure arrays upon illumination through interpost communication. **Left:** Experiment and simulation of the self-organization of the array of closely packed microposts with Z-aligned mesogens into an undulating line. Note that \mathbf{G}_{array} and \mathbf{L} are slightly misaligned (by a small angle δ , Supplementary Figure 25, Manuscript Figure 4a & b). **Right:** Different self-organized patterns form by slightly changing δ . Note that indicated angles of illumination are exaggerated for illustration purposes (Supplementary Figure 29).

Supplementary Video 7 | Spacing-dependent interpost communication in 2D pillar arrays. **Left:** In square 2D arrays, changing the illumination from the nearest-neighbor direction to diagonal influences the presence or absence of interpost communication and collective behavior (Manuscript Figure 4c). **Right:** Irradiation of a circular array of microposts creates collective deformation dynamics, in which a global deformation front travels concurrently (with a different propagation velocity) across the array shaped by the locally changing interpost spacing and different \mathbf{G}_a -axes (Manuscript Figure 4d).

Supplementary Video 8 | Amplification of ‘defects’ in arrays of microposts with oblique mesogen alignment: missing posts alter the interpost spacing and dramatically change the deformation trajectories of neighboring posts and thus the overall collective deformation dynamics (Manuscript Figure 4e). Note the similar behavior of the ‘effective first row’ (denoted by red circles).

Supplementary Video 9 | Photoresponse of jointed microstructures. **Left:** A free-standing V-shaped jointed microstructure with a director alignment of $+45^\circ$ and -45° relative to the two respective segments (arms) exhibits simultaneous bending and twisting motions of opposite direction for the two arms (Supplementary Figure 33). **Middle:** The directionality of these motions can be programmed through director orientation, as an X-shaped actuator (anchored at its center) demonstrates (Supplementary Figure 34, Manuscript Figure 5a,i). **Right:** If an X-shaped actuator is anchored at the end of one segment, its twisting motion amplifies through the horizontal branching arm (Manuscript Figure 5a,i).

Supplementary Video 10 | Simulation results of the photoresponsive behavior of L-, V-, T-, & palm-tree-shaped LCE microactuators (Supplementary Figure 31) with horizontal, vertical, or oblique global director alignment exhibiting a range of non-trivial motions interesting for soft robotic applications.

5 References

1. Seebach, D., Imwinkelried, R. & Stucky, G. Optisch Aktive Alkohole aus 1,3-Dioxan-4-onen: Eine Praktikable Variante der Enantioselektiven Synthese unter Nucleophiler Substitution an Acetal-Zentren. *Helv. Chim. Acta* **70**, 448–464 (1987).
2. Fulmer, G. R., Miller, A. J. M., Sherden, N. H., Gottlieb, H. E., Nudelman, A., Stoltz, B. M., Bercaw, J. E. & Goldberg, K. I. NMR chemical shifts of trace impurities: Common laboratory solvents, organics, and gases in deuterated solvents relevant to the organometallic chemist. *Organometallics* **29**, 2176–2179 (2010).
3. Thomsen, D. L., Keller, P., Naciri, J., Pink, R., Jeon, H., Shenoy, D. & Ratna, B. R. Liquid crystal elastomers with mechanical properties of a muscle. *Macromolecules* **34**, 5868–5875 (2001).
4. Chandra, D., Taylor, J. A. & Yang, S. Replica molding of high-aspect-ratio (sub-)micron hydrogel pillar arrays and their stability in air and solvents. *Soft Matter* **4**, 979–984 (2008).
5. Zhang, Y., Lo, C. W., Taylor, J. A. & Yang, S. Replica molding of high-aspect-ratio polymeric nanopillar arrays with high fidelity. *Langmuir* **22**, 8595–8601 (2006).
6. Yao, Y., Waters, J. T., Shneidman, A. v, Cui, J., Wang, X., Mandsberg, N. K., Li, S., Balazs, A. C. & Aizenberg, J. Multiresponsive polymeric microstructures with encoded predetermined and self-regulated deformability. *Proc. Natl. Acad. Sci. USA* **115**, 12950–12955 (2018).
7. Gennes, P.-G. de. *The physics of liquid crystals*. (Clarendon Press, 1993).
8. Buguin, A., Li, M. H., Silberzan, P., Ladoux, B. & Keller, P. Micro-actuators: When artificial muscles made of nematic liquid crystal elastomers meet soft lithography. *J. Am. Chem. Soc.* **128**, 1088–1089 (2006).
9. Demus, D., Goodby, J. W., Gray, G. W., Spiess, H. W. & Vill, V. *Handbook of Liquid Crystals*. **2**, (Wiley-VCH, 2011).
10. Waters, J. T., Li, S., Yao, Y., Lerch, M. M., Aizenberg, M., Aizenberg, J. & Balazs, A. C. Twist again: Dynamically and reversibly controllable chirality in liquid crystalline elastomer microposts. *Sci. Adv.* **6**, eaay5349 (2020).
11. Corbett, D., van Oosten, C. L. & Warner, M. Nonlinear dynamics of optical absorption of intense beams. *Phys. Rev. A* **78**, 13823 (2008).
12. Beer, F. P., Johnston, E. R., DeWolf, J. T., Mazurek, D. F. & Sanghi, S. *Mechanics of materials*. (McGraw-Hill, 2020).
13. Gelebart, A. H., Vantomme, G., Meijer, E. W. & Broer, D. J. Mastering the photothermal effect in liquid crystal networks: A general approach for self-sustained mechanical oscillators. *Adv. Mater.* **29**, 1606712 (2017).
14. Gelebart, A. H., Jan Mulder, D., Varga, M., Konya, A., Vantomme, G., Meijer, E. W., Selinger, R. L. B. & Broer, D. J. Making waves in a photoactive polymer film. *Nature* **546**, 632–636 (2017).
15. Pilz da Cunha, M., van Thoor, E. A. J., Debije, M. G., Broer, D. J. & Schenning, A. P. H. J. Unravelling the photothermal and photomechanical contributions to actuation of azobenzene-doped liquid crystal polymers in air and water. *J. Mater. Chem. C* **7**, 13502–13509 (2019).
16. Page, R. M. Light and the asexual reproduction of pilobolus. *Science* **138**, 1238–1245 (1962).